THESIS FOR THE DEGREE OF LICENTIATE OF PHILOSOPHY

# Microscopic Mechanisms of the Formation, Relaxation and Recombination of Excitons in Two-Dimensional Semiconductors

Samuel Brem


Department of Physics

Chalmers University of Technology

Göteborg, Sweden 2019

Microscopic Mechanisms of the Formation, Relaxation and Recombination of Excitons in Two-Dimensional Semiconductors

Samuel Brem



Department of Physics
Chalmers University of Technology
SE-412 96 Göteborg
Sweden
Telephone + 46 (0)31-772 1000



Printed at Chalmers Reproservice
Göteborg, Sweden 2019

Microscopic Mechanisms of the Formation, Relaxation and Recombination of Excitons in Two-Dimensional Semiconductors

Samuel Brem
Department of Physics
Chalmers University of Technology

## Abstract

Monolayers of Transition Metal Dichalcogenides (TMDs) present a giant leap forward towards the realization of semiconductor devices with atomic scale thickness. As a natural consequence of their two-dimensional character TMDs exhibit a reduced dielectric screening, leading to the formation of unusually stable excitons, i.e. Coulomb-bound electron-hole pairs. Excitons dominate the optical response as well as the ultrafast dynamics in TMDs. As a result, a microscopic understanding of excitons, their formation, relaxation and decay dynamics becomes crucial for a technological application of TMDs. A detailed theoretical picture of the internal structure of excitons and their scattering channels allows for a controlled manipulation of TMD properties enabling an entire new class of light emitters and detectors.
The aim of this thesis is to investigate the many-particle processes governing the ultrafast dynamics of excitons. The focus is to provide a sophisticated picture of exciton-phonon and exciton-photon interaction mechanisms and the impact of dark exciton states starting from the formation of bound excitons out of a free electron-hole gas up to the eventual radiative decay of bright and dark exciton populations. Based on an equations-of-motion approach for the density matrix of an interacting electron, phonon and photon system, we simulate the dynamics of excitons in TMDs across the full Rydberg-like series of bright and dark states. Our theoretical model allows us to predict fundamental relaxation time scales as well as spectral features accessible in multiple spectroscopic experiments, such as absorption, photoluminescence and ultrafast pump-probe. In particular we predict intriguing features appearing in the terahertz absorption spectrum during the formation of excitons as well as distinct -so far unexplained- low temperature luminescence features stemming from phonon-assisted recombinations of dark excitons.

**Keywords:** excitons, density matrix formalism, Bloch equations, 2D materials, relaxation dynamics, exciton-phonon interaction

## List of publications

This thesis consists of an introductory text and the following papers:

I. **Exciton Relaxation Cascade in two-dimensional Transition Metal Dichalcogenides**
S Brem, M Selig, G Berghäuser and E Malic
Scientific reports 8.1: 8238 (2018)

II. **Intrinsic Lifetime of Higher Excitonic States in Tungsten Diselenide Monolayers**
S Brem, J Zipfel, M Selig, A Raja, L Waldecker, J Ziegler, T Taniguchi, K Watanabe, A Chernikov, E Malic
arXiv preprint arXiv:1904.04729 (2019)

III. **Phonon-assisted Photoluminescence from Dark Excitons in Monolayers of Transition Metal Dichalcogenides**
S Brem, A Ekman, D Christiansen, F Katsch, M Selig, C Robert, X Marie, B Urbaszek, A Knorr, E Malic
arXiv preprint arXiv:1904.04711 (2019)

**My contributions to the appended papers**
As first-author, I developed the theoretical model, performed the numerical evaluation, analyzed the results and wrote the papers with the help of my main supervisor.

# Publications not appended in this thesis:

IV. **Microscopic modeling of tunable graphene-based terahertz Landau-level lasers**
S Brem, F Wendler, E Malic
Physical Review B 96 (4), 045427 (2017)

V. **Symmetry-breaking supercollisions in Landau-quantized graphene**
F Wendler, M Mittendorff, JC König-Otto, S Brem, C Berger, WA de Heer, R Böttger, H Schneider, M Helm, S Winnerl, E Malic
Physical review letters 119 (6), 067405 (2017)

VI. **Carrier Dynamics in Graphene: Ultrafast Many-Particle Phenomena**
E Malic, T Winzer, F Wendler, S Brem, R Jago, A Knorr, M Mittendorff, JC König-Otto, T Plötzing, D Neumaier, H Schneider, M Helm, S Winnerl
Annalen der Physik 529 (11), 1700038 (2017)

VII. **Dark excitons in transition metal dichalcogenides**
E Malic, M Selig, M Feierabend, S Brem, D Christiansen, F Wendler, A Knorr, G Berghäuser
Physical Review Materials 2 (1), 014002 (2018)

VIII. **Molecule signatures in photoluminescence spectra of transition metal dichalcogenides**
M Feierabend, G Berghäuser, M Selig, S Brem, T Shegai, S Eigler, E Malic
Physical Review Materials 2 (1), 014004 (2018)

IX. **Dielectric engineering of electronic correlations in a van der waals heterostructure**
P Steinleitner, P Merkl, A Graf, P Nagler, K Watanabe, T Taniguchi, J Zipfel, C Schüller, T Korn, A Chernikov, S Brem, M Selig, G Berghäuser, E Malic, R Huber
Nano letters 18 (2), 1402-1409 (2018)

X. **Electrically pumped graphene-based Landau-level laser**
S Brem, F Wendler, S Winnerl, E Malic
Physical Review Materials 2 (3), 034002 (2018)

XI. **Impact of strain on the excitonic linewidth in transition metal dichalcogenides**
Z Khatibi, M Feierabend, M Selig, S Brem, C Linderälv, P Erhart, E Malic
2D Materials 6 (1), 015015 (2018)

XII. **Interlayer exciton dynamics in van der Waals heterostructures**
S Ovesen, S Brem, C Linderälv, M Kuisma, T Korn, P Erhart, M Selig, E Malic
Communications Physics 2 (1), 23 (2019)

XIII. **The influence of disorder in the external environment of 2D semiconductors on their electronic and optical properties**
A Raja, L Waldecker, J Zipfel, Y Cho, S Brem, J Ziegler, T Taniguchi, K Watanabe, E Malic, T Berkelbach, T Heinz, A Chernikov
Bulletin of the American Physical Society (2019)

XIV. **Spatio-temporal dynamics in graphene**
R Jago, R Perea-Causin, S Brem, E Malic
arXiv preprint arXiv:1903.12420 (2019)

XV. **Disorder-induced broadening of excitonic resonances in transition metal dichalcogenides**
M Dwedari, S Brem, M Feierabend, E Malic
under review (2019)

XVI. **Ultrafast transition between exciton phases in van der Waals heterostructures**
P Merkl, F Mooshammer, P Steinleitner, A Girnghuber, K-Q Lin, P Nagler, J Holler, C Schüller, JM Lupton, T Korn, S Ovesen, S Brem, E Malic, R Huber
Nature materials, 1 (2019)

**My contributions to the papers**
As first-author in IV and X, I developed the theoretical model, performed the numerical evaluation, analyzed the results and wrote the paper with the help of my main supervisor. In the other publications I contributed by performing specific calculations and/or analyzing and interpreting results.

# Contents

# 1 Introduction

The ongoing miniaturization of electronic technologies has nowadays reached fundamental limitations. Conventional concepts for semiconductor-based devices often break down when the length scale of critical components reaches the nanometre regime, in which quantum effects become dominant. However, a new class of so-called quantum materials present a chance to overcome these limitations and eventually even enable completely new paradigms for information storage and processing, such as spin- and valleytronics [1, 2].

In particular, two-dimensional crystals with the thickness of a few atoms, so called monolayers have attracted tremendous attention in research over the last ten years. The first experimental realization of graphene (carbon monolayers) has been awarded with the Nobel prize in 2010 and the subsequent boom in 2D materials research has lead to the discovery of a large library of stable monolayer materials [3–6], including the semiconducting family of transition metal dichalcogenides (TMDs) [7]. This new class of semiconductors exhibits a variety of outstanding physical properties, which are advantageous not only for technological applications [8–11], but also for fundamental research of correlated quantum systems [12].

Since TMDs are quasi two-dimensional, they exhibit a reduced dielectric screening, which consequently leads to the formation of unusually stable excitons [13–15], i.e. Coulomb-bound electron-hole pairs. These quasi-particles dominate the optical characteristics of TMDs [16–18], so that a microscopic understanding of excitons becomes of crucial importance for TMD-based technologies. Moreover, the large exciton binding energies in TMDs facilitate the study of the exciton Rydberg series and intra-excitonic transitions [19–21], which was technologically limited in conventional platforms used for the study of exciton physics, such as GaAs quantum wells. A detailed theoretical picture of the internal structure of excitons and their scattering channels might enable a controlled manipulation of TMD properties and thereby an entire new class of light emitters and absorbers.

The aim of this thesis is to investigate the many-particle processes governing the temporal dynamics of excitons in TMDs. The focus hereby is to provide a sophisticated picture of exciton-phonon and exciton-photon interaction mechanisms, starting from the formation of bound excitons out of a

free electron-hole gas, up to the eventual radiative decay of different exciton species. To this end we use a density matrix approach to calculate the dynamics of an interacting system of electrons, phonons and photons. Thereby, we can map the trajectory of excitons through their energy landscape which allows for a microscopic interpretation of recent experiments performed on TMDs. Our model predicts fundamental relaxation timescales of excitons as well as spectral features accessible in multiple spectroscopic experiments, such as absorption, photoluminescence and ultrafast pump-probe.

# 2 Transition Metal Dichalcogenides

In the following section we first consider the – for this thesis relevant – physical properties of TMD monolayer crystals. The second part of this section introduces the mathematical framework used to include the material specific properties into a general many-particle quantum theory presented in Sec. 3.

## 2.1 Crystal Symmetry and Electronic Band Structure

TMD monolayers are composed by a central plane of transition metal atoms (often Mo or W) sandwiched by two planes of chalcogen atoms (S or Se), which are covalently bond to the neighbouring metal atoms [22]. In a top view, the atoms are arranged in a hexagonal honeycomb lattice with alternating atomic species on the lattice sites, cf. Fig. 1a. The corresponding hexagonal Brillouin zone of the reciprocal lattice is displayed in Fig. 1b showing the definition of relevant high symmetry points. Due to the fact that the unit cell of TMDs contains two atoms, we find two inequivalent corners of the Brillouin zone denoted K and K'. The generic form of the electronic band structure in TMD monolayers is shown along the symmetry path in Fig. 1c. Most importantly, we find a direct band gap at the K point [23] which exhibits a significant splitting denoted $\Delta_{cb}$ and $\Delta_{vb}$, between differently spin-polarized bands, which results from the large magnetic momentum of the transition metal d orbitals constituting the corresponding Bloch waves. Interestingly, as a result of time-reversal symmetry, the energetic ordering of the spin-split bands is inverted at K and K' points. Together with the special optical selection rules discussed in Sec. 2.4 this facilitates the optical excitation of spin- and valley polarized excitons in TMDs [24–28]. Apart from the K point, there is another local minimum of the conduction band at the $\Lambda$ point, which is also often referred to as Q point. Due to its close energetic proximity to the conduction band edge at the K point, the $\Lambda$ point can play an important role for transport and optical characteristics of TMDs [29–32], since it presents an efficient scattering channel as will be shown in this thesis.

Instead of considering the complex band structure across the full Brillouin

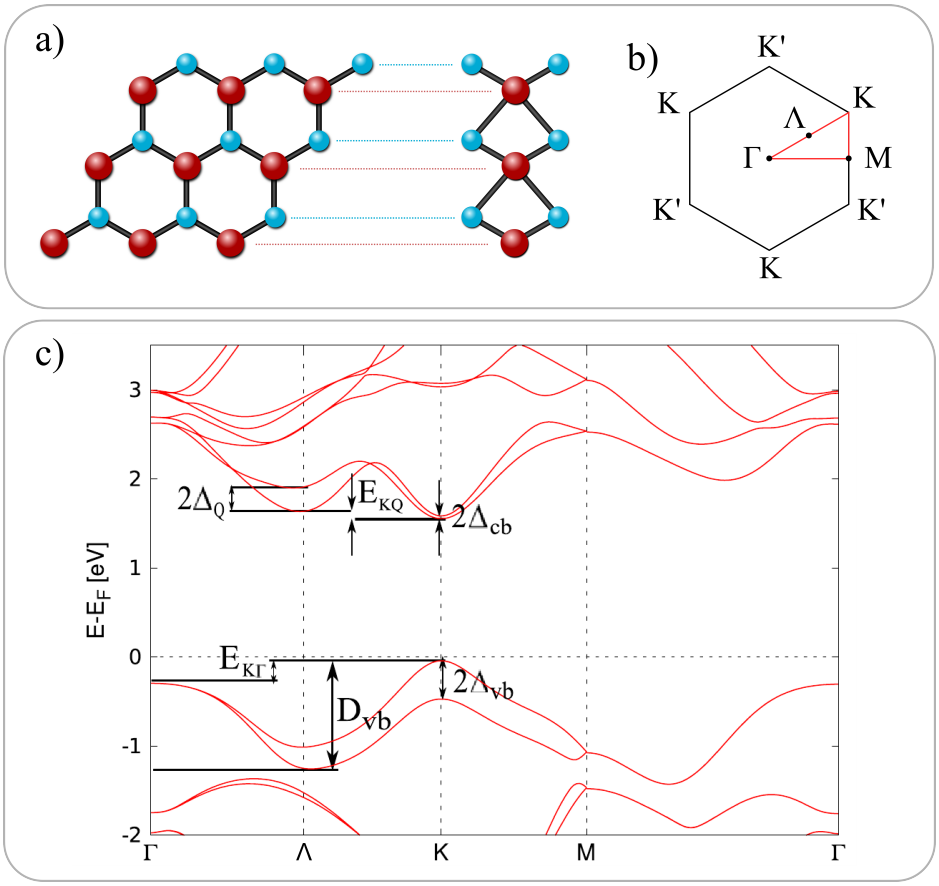


Figure 1: Overview of crystal properties in TMDs. a) top and side view of the hexagonal lattice structure. A layer of transition-metal atoms (blue) is sandwiched by two layers of chalcogen atoms (yellow). b) Corresponding first Brillouin zone together with important high-symmetry points. c) Typical electronic band structure of a TMD monolayer along the high-symmetry lines calculated with DFT. Figure c) is adopted from Ref. [23].

zone, we will throughout this work apply simplified, effective models which are valid in vicinity of minima and maxima of the valence and conduction band. Thereby, material specific properties will enter via effective masses and electronic valley distances extracted from full density functional theory (DFT) in ref. [23].

## 2.2 Tight-binding approach

A convenient way to introduce the general lattice symmetry into an effective model of the electronic properties, is to describe the lattice wave functions $\Psi_{\mathbf{k}}$ with momentum $\mathbf{k}$ in the tight binding approach [33, 34]

$$\Psi_{\mathbf{k}}(\mathbf{r}) = \sum_{l=1,2} c^l_{\mathbf{k}} \psi^l_{\mathbf{k}}(\mathbf{r}) = \frac{1}{\sqrt{N}} \sum_{l=1,2} c^l_{\mathbf{k}} \sum_{\mathbf{R}_l} e^{i\mathbf{k}\mathbf{R}_l} \Phi^l(\mathbf{r} - \mathbf{R}_l). \tag{2.1}$$

Here we sum over the two sub-lattices $l$, whose wave functions are written as superposition of atomic orbitals $\Phi$ localized at the respective lattice sites $\mathbf{R}_l$. Note that the analysis of wave functions obtained from DFT shows that the dominant orbital contribution to the wave function of valence and conduction band change throughout the Brillouin zone. While the conduction band at the K point is well described by superposition of $d_z$ orbitals, the wave function at the $\Lambda$ point inherits the symmetry of $d_x$ and $d_y$ orbitals [23]. Therefore, the following consideration is only valid in close vicinity of certain high symmetry points.

Using Eq. 2.1 we can rewrite the Schrödinger equation into an algebraic problem,

$$\sum_{l'} H^{ll'}_{\mathbf{k}} c^{l'}_{\mathbf{k}} = \varepsilon_{\mathbf{k}} \sum_{l'} S^{ll'}_{\mathbf{k}} c^{l'}_{\mathbf{k}}, \tag{2.2}$$

with $H^{ll'}_{\mathbf{k}} = \langle \psi^l_{\mathbf{k}} | H | \psi^{l'}_{\mathbf{k}} \rangle$ and $S^{ll'}_{\mathbf{k}} = \langle \psi^l_{\mathbf{k}} | \psi^{l'}_{\mathbf{k}} \rangle$. With Eq. 2.1 these integrals can be further decomposed into atomic interaction and overlap integrals. Taking into account only the interaction between the nearest neighbors, we find

$$H^{ll'}_{\mathbf{k}} = E^l \delta_{ll'} + \gamma f(\mathbf{k})(1 - \delta_{ll'}); \qquad f(\mathbf{k}) = \sum_{\mathbf{b}_j} e^{i\mathbf{k}\mathbf{b}_j} \tag{2.3}$$

$$S^{ll'}_{\mathbf{k}} = \delta_{ll'}, \tag{2.4}$$

with the atomic energy $E^l = \langle \Phi^l | H | \Phi^l \rangle$, the inter-atomic matrix element $\gamma = \langle \Phi^1 | H | \Phi^2 \rangle$ and the next neighbour connection vectors $\mathbf{b}_j$ introducing the lattice geometry into the problem. With the above approximations, di-

agonalizing Eq. 2.2 yields,

$$\varepsilon_{\lambda\mathbf{k}} = \bar{E}_{12} + \lambda\sqrt{\gamma^2|f(\mathbf{k})|^2 + (\Delta/2)^2} \tag{2.5}$$

$$c^{(1)}_{\lambda\mathbf{k}} = \lambda\frac{f(\mathbf{k})}{|f(\mathbf{k})|}c^{(2)}_{-\lambda,\mathbf{k}}; \quad c^{(2)}_{\lambda\mathbf{k}} = \frac{1}{2}\sqrt{1 - \frac{\Delta}{2(\varepsilon_{\lambda\mathbf{k}} - \bar{E}_{12})}}, \tag{2.6}$$

where we have abbreviated the energy offset $\bar{E}_{12} = 1/2(E^1 + E^2)$ and the band gap $\Delta = E^1 - E^2$. Here the function $f(\mathbf{k})$ contains all the information about the hexagonal lattice and gives rise to energetic minima (maxima) of the conduction band $\lambda = +1$ (valence band $\lambda = -1$) at the K and K' point. We can now adjust the open parameters in Eq. 2.6 to obtain the band gap and band curvature at the K-point from DFT calculations. The great advantage of having an analytical expression for the components in Eq. 2.6 is that we can now compute important interaction matrix elements in TMDs, by taking into account the hexagonal lattice symmetry, and at the same time keeping the model as simple as effective mass descriptions using plane waves as a basis.

## 2.3 Effective Hamiltonian

To further simplify the model Hamiltonian we apply a Taylor expansion of $f$ in vicinity of $\xi K$ points ($\xi = +1 \to K$; $\xi = -1 \to -K = K'$):

$$f(\mathbf{k} \approx \xi K) \approx \sqrt{3}/2a_0(\xi\tilde{k}_x - i\tilde{k}_y); \quad \tilde{\mathbf{k}} = \mathbf{k} - \xi K \tag{2.7}$$

yielding an effective Hamiltonian in the form of a 2D Dirac particle [35]

$$\mathcal{H}^{\text{eff}}_{\xi\mathbf{k}} = \begin{pmatrix} \Delta/2 & a_0t(\xi k_x - ik_y) \\ a_0t(\xi k_x + ik_y) & -\Delta/2 \end{pmatrix} \tag{2.8}$$

$$= \frac{\Delta}{2}\sigma_z + a_0t(\xi k_x\sigma_x + k_y\sigma_y) \tag{2.9}$$

with $t$ beeing the effective next neighbour hopping parameter. Comparing the bandstructure resulting from the effective Hamiltonian with the generic parabolic bandstructure of a semiconductor we find $t \approx \hbar/a_0\sqrt{\Delta/(m_c + m_v)}$.

The eigenvectors of this Hamiltonian are referred to as pseudo-valley spinors

$$\Psi^{(c)}_{\xi\mathbf{k}} = \begin{pmatrix} c^{(1)}_{c,\mathbf{k}} \\ c^{(2)}_{c,\mathbf{k}} \end{pmatrix} \approx \begin{pmatrix} \xi e^{-i\xi\theta_{\mathbf{k}}} \\ 0 \end{pmatrix}; \qquad \Psi^{(v)}_{\xi\mathbf{k}} \approx \begin{pmatrix} 0 \\ 1 \end{pmatrix}, \tag{2.10}$$

reducing the influence of our particular lattice geometry to a phase in the effective valley wave function. This phase gives rise to a non-zero valley winding numbers (Berry phase), which is connected to interesting topological effects in TMDs [26]. However, we will later demonstrate, that it does not affect the scattering dynamics of excitons in close vicinity of the Dirac points.

## 2.4 Interaction Matrix Elements

Based on the above described effective Hamiltonian and wave functions, we can now find important matrix elements for the quantification of different interaction mechanisms in TMDs. The interaction with light is directly proportional to the inter-band momentum matrix element [35],

$$\begin{aligned} \mathbf{M}^{vc}_{\mathbf{k}} &= -i\hbar\langle v\mathbf{k}|\nabla|c\mathbf{k}\rangle = \frac{m_0}{\hbar}\Psi^{(v)\dagger}_{\xi\mathbf{k}}(\frac{\partial}{\partial\mathbf{k}}\mathcal{H}^{\text{eff}}_{\xi\mathbf{k}})\Psi^{(c)}_{\xi\mathbf{k}} \\ &\approx \frac{m_0}{\hbar}a_0 t e^{-i\xi\theta_{\mathbf{k}}}\begin{pmatrix} 1 \\ i\xi \end{pmatrix}. \end{aligned} \tag{2.11}$$

Most importantly, we find that the matrix element is proportional to a $\sigma(\xi)$-polarized Jones vector. The coupling strength to the light field is given by the projection of the field polarization to the momentum matrix element (cf. section 3). Therefore we can directly deduce a so called *circular valley dichroism* [25, 26, 35] from Eq. 2.11. While the K-valley only couples to $\sigma-$ light, K' is only excited by $\sigma+$ polarization.

Another important quantity characterizing the strength of all scattering mechanisms is the scattering form factor, which for small momentum transfers $\mathbf{q}$ can be derived in next neighbour approximation:

$$\begin{aligned} \mathcal{F}^{\lambda}_{\mathbf{k}\mathbf{k}'}(\mathbf{q}) &= \langle\lambda\mathbf{k}|e^{i\mathbf{q}\mathbf{r}}|\lambda\mathbf{k}'\rangle = \delta_{\mathbf{k}'-\mathbf{k},\mathbf{q}}\Psi^{(\lambda)\dagger}_{\xi\mathbf{k}}\Psi^{(\lambda)}_{\xi\mathbf{k}'} \\ &\approx \delta_{\mathbf{k}'-\mathbf{k},\mathbf{q}}\begin{cases} e^{i\xi(\theta_{\mathbf{k}}-\theta_{\mathbf{k}'})} & \text{for } \lambda = c \\ 1 & \text{for } \lambda = v \end{cases} \end{aligned} \tag{2.12}$$

## 2.5 Dielectric Screening in two-dimensional Subsystems

One of the most important difference between monolayers and conventional quasi-2D systems such as quantum wells, is the maximal confinement of electrons to a plane and the resulting strong modification of the dielectric screening [36, 37]. Figure 2 illustrates the difference between the field lines in a 3D system and 2D system embedded into a 3D environment [37]. In a bulk

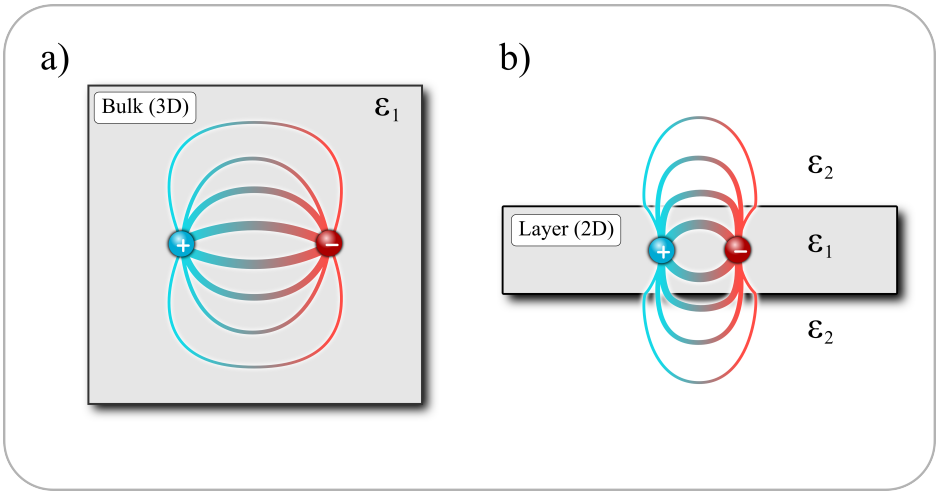


Figure 2: Dielectric Screening in a) bulk and b) monolayer. While in bulk systems the field lines between interacting charges penetrate the surrounding crystal, in the case of monolayers most field lines expand in vacuum or materials with lower dielectric constants, giving rise to a weaker screening in two-dimensional systems. Illustration inspired by Ref. [37].

system (Fig. 2a) the field lines between two attracting charges penetrate the surrounding material and become weakened by the induced polarization. In contrast, for the 2D system, most field lines penetrate the space surrounding the monolayer and therefore -in the case of low dielectric constant- become much less weakened than in the bulk material. Moreover, the resulting distance behaviour of the effective Coulomb potential becomes a mixture of 2D and 3D components. To determine the potential $V(\mathbf{r})$ we apply a fully classical approach, assuming point charges localized in the centre ($z = 0$) of a homogeneous dielectric slab with thickness $d$. In this picture the potential

can be determined by the first Maxwell equation:

$$\nabla \mathbf{D} = -e_0\delta(\mathbf{r}); \quad \mathbf{D} = -\epsilon_0/e_0 \sum_{i=1,2,3} \epsilon^i(\mathbf{r})\partial_i V(\mathbf{r}) \tag{2.13}$$

$$\epsilon^i(\mathbf{r}) = \begin{cases} \epsilon_1^i & \text{for } |z| \leq d/2 \\ \epsilon_2^i & \text{for } |z| > d/2 \end{cases} \tag{2.14}$$

where the second line defines the dielectric landscape through the dielectric tensor of the TMD ($\epsilon_1$) and the environment($\epsilon_2$). Using Gauss's divergence theorem, we can determine conditions for the field at the boundary of the slab, yielding the 2D Fourier transformed potential (at $z = 0$)

$$V_{\mathbf{q}} = \frac{e_0^2}{2\epsilon_0 q \epsilon_{\mathrm{s}}(q)}; \qquad \epsilon_{\mathrm{s}}(q) = \kappa_1 \tanh(\frac{1}{2}[\alpha_1 dq - \ln(\frac{\kappa_1 - \kappa_2}{\kappa_1 + \kappa_2})]) \tag{2.15}$$

whith $\kappa_i = \sqrt{\epsilon_i^{\parallel}\epsilon_i^{\perp}}$ and $\alpha_i = \sqrt{\epsilon_i^{\parallel}/\epsilon_i^{\perp}}$.

In the limiting case of small momenta $dq << 1$ and large dielectric contrast $\epsilon_1 >> \epsilon_2$ the potential can be approximated with the Keldysh form [38, 39]

$$V_{\mathbf{q}} = \frac{e_0^2}{2\epsilon_0 q(\kappa_2 + \epsilon_1^{\parallel} dq/2)} \tag{2.16}$$

Hence, for small wave vectors (large distances) we obtain an effective 2D distance dependence ($1/q$) only screened by the environment, while at larger wave vectors (small distances) the potential becomes more 3D ($1/q^2$) with increasing influence of the TMD screening. Throughout this thesis we use dielectric constants for TMD monolayers obtained from DFT calculations [40].

# 3 Many-Particle Quantum Theory

In the following section we introduce the general theoretical framework applied throughout this thesis. In the first part the many-particle density matrix approach is introduced and discussed. The second part focusses on the approximations used in this work to reduce the mathematical complexity of the problem. In principle the shown framework can be applied to model the excitation kinetics of an arbitrary system of interacting electrons, phonons and photons.

## 3.1 Canonical Quantization

In order to describe the quantized interaction between different degrees of freedom, we have to use a theoretical model unifying the different properties of light (photons), matter (here electrons) and lattice vibrations (phonons). The quantum field theory has proven to be a powerful tool for treating many-particle problems in condensed matter [41–44]. Here, the canonical quantization scheme is used to transform classical field theories into a many-particle quantum theory, by replacing Poisson brackets with commutators.

### Photons

To obtain a quantized theory of the electromagnetic field (in Coulomb gauge) the vector potential $\mathbf{A}$ is transformed to an operator acting on wave functions in Fock space,

$$\mathbf{A}(\mathbf{r},t) \longrightarrow \hat{\mathbf{A}}(\mathbf{r},t) = \sum_{\sigma\mathbf{k}} \sqrt{\frac{\hbar}{2\epsilon_0 L^3 \omega_k}} \mathbf{e}_{\sigma\mathbf{k}} c_{\sigma\mathbf{k}}(t) e^{i\mathbf{kr}} + \text{h.a.} \tag{3.1}$$

Here $c^{(\dagger)}_{\sigma\mathbf{k}}$ annihilates (creates) a photon in mode $\sigma$, wavevector $\mathbf{k}$, polarization $\mathbf{e}_{\sigma\mathbf{k}}$ and frequency $\omega_k = ck$. From the fundamental commutation relation, $[x,p] = i\hbar$ generalized to field coordinate and field momentum [45] we find the bosonic properties of the photon

$$[c_{\sigma\mathbf{k}},c_{\sigma'\mathbf{k}'}] = [c^\dagger_{\sigma\mathbf{k}},c^\dagger_{\sigma'\mathbf{k}'}] = 0; \quad [c_{\sigma\mathbf{k}}(t),c^\dagger_{\sigma'\mathbf{k}'}(t)] = \delta_{\sigma\sigma'}\delta_{\mathbf{kk}'} \tag{3.2}$$

Moreover, the Hamiltonian of the electromagnetic field obtains the convenient form

$$H = \int d^3r[\frac{1}{2}\epsilon_0(\partial_t\hat{\mathbf{A}})^2 + \frac{1}{\mu_0}(\nabla\times\hat{\mathbf{A}})^2] \tag{3.3}$$

$$= \sum_{\sigma\mathbf{k}}\hbar\omega_k(c^\dagger_{\sigma\mathbf{k}}c_{\sigma\mathbf{k}} + \frac{1}{2}) \tag{3.4}$$

Hence, each mode of the electromagnetic field can be interpreted as a harmonic oscillator with a quantized energy given by the integer number of photons $\langle c^\dagger_{\sigma\mathbf{k}}c_{\sigma\mathbf{k}}\rangle$ in that mode.

### Phonons

Similar to the electromagnetic field, we can quantize the collective lattice vibrations in a crystal. The motion within a lattice of $N$ interacting atoms can be described with the classical Hamiltonian,

$$H = \sum_{i=1}^{N}\frac{\mathbf{p}_i^2}{2M} + \sum_{i,j}\mathbf{u}_i\cdot\underline{\Theta}^{ij}\cdot\mathbf{u}_j, \tag{3.5}$$

where $\mathbf{p}_i$ is the momentum of the $i$th particle and $\mathbf{u}_i$ is a small deviation from its rest position $\mathbf{R_i}$. The dynamical matrix $\underline{\Theta}^{ij}$ contains the forces between all particles resulting from the repulsion of their nuclei and the attraction mediated by the core and valence electrons. By diagonalising the dynamical matrix, we can find the collective eigenmodes $(\alpha,\mathbf{q})$ of the system, which are subsequently quantized,

$$\mathbf{u}_i(t) \longrightarrow \hat{\mathbf{u}}_i(t) = \frac{1}{N}\sum_{\alpha\mathbf{q}}\sqrt{\frac{\hbar}{2M\Omega_{\alpha\mathbf{q}}}}\mathbf{e}_{\alpha\mathbf{q}}b_{\alpha\mathbf{q}}(t)e^{i\mathbf{q}\mathbf{R}_i} + \text{h.a.} \tag{3.6}$$

in terms of phonon operators $b_{\alpha\mathbf{q}}$, creating or annihilating energy quanta of size $\hbar\Omega_{\alpha\mathbf{q}}$ in the respective mode. The corresponding commutation relations and the form of the quantized Hamiltonian are completely analogue to the case of photons.

**Fermions in second Quantization**

For the description of interactions between e.g. light and matter, it is convenient to express the electronic part of the system in terms of creation and annihilation operators as well. Moreover, many-particle quantum theories for massive particles have to take into account the Pauli exclusion principle. While systems of two or three particles might be treated by using anti-symmetric products of single particle wave functions, the Schroedinger equation of $10^9$ particles (typical excitation number per cm$^2$ in a semiconductor) is simply not manageable. However, we can find a similar field theoretical description of electrons as for phonons and photons, by treating the Schroedinger equation as a classical field theory, to which the canonical quantization scheme is applied. Choosing a "classical" Hamiltonian [46],

$$H = \int d^3r \Psi^*(\mathbf{r},t)[-\frac{\hbar}{2m_0}\Delta + V(\mathbf{r})]\Psi(\mathbf{r},t), \tag{3.7}$$

directly yields the Schroedinger equation as the corresponding equation of motion with $\Psi$ as generalized field coordinate and $i\hbar/2\Psi^*$ as field momentum. The quantization now follows from defining field operators $\Psi \rightarrow \hat{\Psi}$ with fermionic anti-commutators to obey the Pauli principle,

$$\{\hat{\Psi}(\mathbf{r},t),\hat{\Psi}^\dagger(\mathbf{r},t)\} = \delta(\mathbf{r}-\mathbf{r}') \tag{3.8}$$

$$\{a_n(t),a_m^\dagger(t)\} = \delta_{nm} \tag{3.9}$$

Where the second line is obtained when expanding the field operator $\hat{\Psi} = \sum \phi_n a_n$ in terms of an orthogonal basis $\{\phi_n\}$. From Eq. 3.7 we can directly deduce a transformation rule for obtaining a Hamiltonian in second quantization from the single particle Hamiltonian $h_1(\mathbf{r})$:

$$H = \sum_{nm} \langle n|h_1|m\rangle a_n^\dagger a_m \tag{3.10}$$

The quantization scheme for two-particle interactions $h_2(\mathbf{r},\mathbf{r}')$ can be obtained in a similar manner by including non-local contributions to the action [46]:

$$H = \frac{1}{2}\sum_{ijkl} \langle ij|h_2|kl\rangle a_i^\dagger a_j^\dagger a_k a_l \tag{3.11}$$

In total the Hamiltonian for an interacting system of electrons reads

$$H = \sum_{\lambda \mathbf{k}} \varepsilon_{\lambda \mathbf{k}} a^\dagger_{\lambda \mathbf{k}} a_{\lambda \mathbf{k}} + \frac{1}{2} \sum_{\lambda \lambda' \mathbf{k} \mathbf{k}' \mathbf{q}} V^{\lambda \lambda'}_{\mathbf{k} \mathbf{k}' \mathbf{q}} a^\dagger_{\lambda \mathbf{k}+\mathbf{q}} a^\dagger_{\lambda' \mathbf{k}'-\mathbf{q}} a_{\lambda' \mathbf{k}'} a_{\lambda \mathbf{k}} \tag{3.12}$$

with the Coulomb matrixelement $V^{\lambda \lambda'}_{\mathbf{k} \mathbf{k}' \mathbf{q}} = V_{\mathbf{q}} \mathcal{F}^{\lambda}_{\mathbf{k}}(\mathbf{q}) \mathcal{F}^{\lambda'}_{\mathbf{k}'}(-\mathbf{q})$, which is determined by the form factors and the Fourier transform of the screened Coulomb potential, both derived in section 2. Note that we assumed very small momenta and the derive Coulomb Hamiltonian corresponds to a monopole approximation. However, under certain conditions the dipole-dipole interaction between electrons can become important, e.g. giving rise to electron-hole exchange interactions, which is neglected throughout this work.

Further details about the canonical quantization scheme can be found in the standard literature about quantum field theory and many-particle physics [47, 48].

## 3.2 Interaction Mechanisms

Based on the quantization scheme for electrons, phonons and photons described above, we can now determine interaction Hamiltonians in second quantization.

### Electron-Light Interaction

Starting point for the description of interactions in second quantization is the single particle Hamiltonian. The interaction of an electron with an external classical electromagnetic field can be introduced into the Schroedinger equation via the so called minimal coupling. Here, we replace the canonical momentum $\mathbf{p}$ with the kinetic momentum $\mathbf{p} + e_0 \mathbf{A}$ in the Hamiltonian introducing the Lorentz force in classical equations of motion. Hence, we find

$$H = \frac{(\mathbf{p} + e_0 \mathbf{A})^2}{2 m_0} = \frac{\mathbf{p}^2}{2 m_0} + \frac{e_0}{2 m_0} (\mathbf{p} \cdot \mathbf{A} + \mathbf{A} \cdot \mathbf{p}) + \frac{e^2}{2 m_0} \mathbf{A}^2. \tag{3.13}$$

In case of irradiation with plane waves with perpendicular wave vector to a monolayer, the vector potential $\mathbf{A}$ does not depend on the spatial coordinate in the monolayer plane. In this case the last term only periodically shifts the overall bandstructure, which has no influence on the dynamics of carriers. Moreover, if $\mathbf{A}$ is homogeneous throughout the sample, it commutes with $\mathbf{p}$ and we find the electron light interaction via

$$h_{\text{el-l}} = \frac{e_0}{m_0}\mathbf{A}\cdot\mathbf{p} \longrightarrow H_{\text{el-l}} = \frac{e_0}{m_0}\sum_{nm}\mathbf{A}\cdot\mathbf{M}_{nm}a_n^\dagger a_m, \tag{3.14}$$

where we have used the transformation rule Eq. 3.10 and the definition $\mathbf{M}_{nm} = -i\hbar\langle n|\nabla|m\rangle$. A fully quantized electron-photon interaction is now obtained by expanding the vector potential in terms of photon operators, cf. Eq. 3.1, which yields

$$H_{\text{el-pt}} = \sum_{nm,\sigma\mathbf{k}} g^{nm}_{\sigma\mathbf{k}} a_n^\dagger a_m c_{\sigma\mathbf{k}} + \text{h.a.}, \qquad g^{nm}_{\sigma\mathbf{k}} = \frac{e_0}{m_0}\sqrt{\frac{\hbar}{2\epsilon_0 L^3\omega_k}}\mathbf{e}_{\sigma\mathbf{k}}\cdot\mathbf{M}_{nm} \tag{3.15}$$

The interpretation of the Hamiltonian is quite intuitive: the creation (emission) or annihilation (absorption) of a photon is accompanied by the transition of an electron between two states. Here, the electron-photon matrix element $g$, which is often referred to as oscillator strength, determines how strong a certain transition couples to the light field.

## Electron-Phonon Interaction

A similar interaction Hamiltonian as for photons can be derived for electrons and phonons. However, here the interaction term is derived from the change in the electronic energies induced by the lattice distortion accompanying the vibration of the crystal. Therefore the electron-phonon matrix is much more sensitive to material properties than in the case of photons and one finds qualitative differences depending on the mode type of the involved phonons. The calculation of material realistic coupling parameters here requires sophisticated computational methods, such as the density functional perturbation theory (DFPT). However, the general form of the interaction Hamiltonian can be obtained by assuming that the electrostatic

potential of the resting crystal lattice can be decomposed into atomic potentials $V^0_{\text{lattice}}(\mathbf{r}) = \sum_i v_{\text{atom}}(\mathbf{r} - \mathbf{R}_i)$. Hence the time dependent potential of the weakly vibrating lattice is approximated via

$$V_{\text{lattice}}(\mathbf{r},t) = V^0_{\text{lattice}}(\mathbf{r}) - \sum_i \nabla v_{\text{atom}}(\mathbf{r} - \mathbf{R}_i) \cdot \mathbf{u}_i(t) \tag{3.16}$$

with small deviations $\mathbf{u}_i$ of the atoms from their rest positions $\mathbf{R}_i$. While the first term in Eq. 3.16 is already included in the electronic bandstructure, the second part represents the electron-phonon Hamiltonina in first quantization. To transfer this term into quantum field theory, we use the expansion of $\mathbf{u}_i$ in terms of phonons, cf. Eq. 3.6, and apply the transformation rule Eq. 3.10 yielding

$$H_{\text{el-ph}} = \sum_{nm,\alpha\mathbf{q}} D^{nm}_{\alpha\mathbf{q}} a^\dagger_n a_m (b_{\alpha\mathbf{q}} + b^\dagger_{\alpha,-\mathbf{q}}) \tag{3.17}$$

$$D^{nm}_{\alpha\mathbf{q}} = -i\sqrt{\frac{N\hbar}{2M\Omega_{\alpha\mathbf{q}}}}\mathbf{q} \cdot \mathbf{e}_{\alpha\mathbf{q}} \tilde{v}_{\text{atom}}(\mathbf{q}) \mathcal{F}_{nm}(\mathbf{q}). \tag{3.18}$$

However, since we do not have access to the exact atomic potentials, we will throughout this work use effective matrix elements deduced from DFPT calculations in ref. [49, 50].

## 3.3 Many-Particle Dynamics

Within the above described formalism, we can now derive the dynamics of an interacting system of electrons, phonons and photons. In particular, we are interested in analysing and explaining experimental results or want to predict the outcome of measurements involving large many-particle systems. In Sec. 5 we will show how certain observables in experiments can be related to expectation values of different particle operator combinations.

### Equations of Motion and Hierachy Problem

To obtain the time evolution of an observable, we apply the Heisenberg equation of motion to the expectation value of the corresponding operator $\mathcal{O}$,

$$i\hbar\partial_t\langle\mathcal{O}\rangle = \langle[\mathcal{O},H]\rangle \tag{3.19}$$

Thereby all relevant operator combinations can be classified by the number of particle transitions they involve [42], viz.

$$\mathcal{O}\{N\} = \beta_1^\dagger..\beta_n^\dagger\alpha_1^\dagger..\alpha_m^\dagger\alpha_1..\alpha_m\beta_1..\beta_l, \quad N = n+m+l. \tag{3.20}$$

Here $\alpha$ and $\beta$ represent an arbitrary fermion and boson operator respectively. Note, that the generic operator above can contain single creation or annihilation of bosons, while each creation of a fermion is accompanied by an annihilation. This restriction results from the fact that our Hamiltonian only contains processes which conserve the total number of fermions, which corresponds to a canonical ensemble in classical mechanics. If we now apply the equation of motion to an N-operator (with $m \neq 0$), the presence of many-particle interactions induces a coupling to an (N+1)-operator. In turn, the equation of motion for (N+1)-operators couple to (N+2)-operators and so forth, giving rise to an infinite hierachy of coupled equations. If we for example want to determined the dynamics of the occupation of a certain fermionic state $|n\rangle$ the electron-phonon contribution yields

$$i\hbar\partial_t\langle a_n^\dagger a_n\rangle\Big|_{\text{el-ph}} = 2\sum_{m,q}\Re\mathrm{e}\Big\{D_q^{nm}\big(\langle a_n^\dagger a_m b_q\rangle + \langle a_n^\dagger a_m b_{-q}^\dagger\rangle\big)\Big\}, \tag{3.21}$$

which connects an electronic single particle observable, to a mixed electron-phonon expectation value. The equation of motion for $\langle a_n^\dagger a_m b_q\rangle$ further couples to even more complex expectation values and so on. In order to solve the equations of motion of a many-particle system, we therefore need a systematic approach to truncate the hierarchy problem.

### Cluster Expansion Approach

An effective way to treat the hierarchy problem is the cluster expansion scheme. Here many-particle expectation values are factorized into products of lower order expectation values and corresponding correction terms, which are a measure for the particle correlations in the system. As an example, a two-particle expectation value $\langle\mathcal{A}\{1\}\mathcal{B}\{1\}\rangle$ would be factorized into single-particle expectation values (singlets) via $\langle\mathcal{A}\mathcal{B}\rangle = \langle\mathcal{A}\rangle\langle\mathcal{B}\rangle + \delta\langle\mathcal{A}\mathcal{B}\rangle$, where $\delta\langle\mathcal{A}\mathcal{B}\rangle$ can be seen as a measure of the correlation between particle $\mathcal{A}$ and particle $\mathcal{B}$. The expansion of an arbitrary N-particle expectation value $\langle N\rangle$

is obtained recursively via [42, 44]

$$\langle 2\rangle = \sum_{\sigma}(-1)^{\sigma_f} P_\sigma \langle 1\rangle\langle 1\rangle + \delta\langle 2\rangle \tag{3.22}$$

$$\langle 3\rangle = \sum_{\sigma}(-1)^{\sigma_f} P_\sigma \langle 1\rangle\langle 1\rangle\langle 1\rangle + \sum_{\sigma}(-1)^{\sigma_f} P_\sigma \langle 1\rangle\delta\langle 2\rangle + \delta\langle 3\rangle \tag{3.23}$$

$$\langle N\rangle = f(\langle 1\rangle, \delta\langle 2\rangle, ..., \delta\langle N\rangle), \tag{3.24}$$

where the sum symbolizes the summation over all unique factorizations of permuted operator sequences and $\sigma_f$ denotes the number of involved permutations of fermionic operators. An important cluster expansion is the so-called Hartree-Fock factorization for electronic operators $a$:

$$\langle a_1^\dagger a_2^\dagger a_3 a_4\rangle = \langle a_1^\dagger a_4\rangle\langle a_2^\dagger a_3\rangle - \langle a_1^\dagger a_3\rangle\langle a_2^\dagger a_4\rangle + \delta\langle a_1^\dagger a_2^\dagger a_3 a_4\rangle \tag{3.25}$$

In principle, the above shown expansion does not represent an approximation and the hierarchy problem will now appear in terms of many-particle correlations. However, in this framework we can now systematically truncate the system of equations by consistently neglecting particle correlations of a certain order. If we for example only take into account single particle expectations values and neglect all appearing correlations, we obtain an effective mean field theory, such as the Hartree-Fock-approximation of the Coulomb interaction. When further accounting for two-particle correlations, we can add contributions describing particle scattering as well as the formation of bound particle configurations, such as excitons.

### Born-Markov-Approximation

In addition to the cluster expansion, we can further reduce the number of relevant equations of motion by using approximative analytical solutions for many-particle correlations. One frequently used approach in the treatment of interacting open quantum systems is the Born-Markov-approximation. Here non-linearities resulting from quantum memory effects are neglected to obtain adiabatic solutions describing instantaneous interactions. In this thesis the Markov-approximation is referred to as a specific mathematical step. The generic form of a Heisenberg equation of motion reads

$$\partial_t \mathcal{X}(t) = (i\omega_0 - \gamma)\mathcal{X}(t) + \mathcal{S}(t), \tag{3.26}$$

which has the formal solution

$$\mathcal{X}(t) = \mathcal{X}(t_0)e^{(i\omega_0-\gamma)(t-t_0)} + \int_{t_0}^{t} d\tau \mathcal{S}(\tau)e^{(i\omega_0-\gamma)(t-\tau)} \tag{3.27}$$

$$= \int_0^{\infty} d\tau \mathcal{S}(t-\tau)e^{(i\omega_0-\gamma)\tau} \tag{3.28}$$

Where the second line results from setting the initial time to $t_0 \longrightarrow -\infty$, so that we can neglect the first term of Eq. 3.27, assuming a fast decay of the initial value of $\mathcal{X}$. Now we assume that the source terms $\mathcal{S}$ can be split into an oscillation with a characteristic frequency $\omega_s$ and a slowly varying envelope $\tilde{\mathcal{S}}$. Hence we find [33]

$$\mathcal{X}(t) = \int_0^{\infty} d\tau \tilde{\mathcal{S}}(t-\tau)e^{[i(\omega_0-\omega_s)-\gamma]\tau+i\omega_s t} \tag{3.29}$$

$$= \tilde{\mathcal{S}}(t)e^{i\omega_s t}\int_0^{\infty} d\tau e^{[i(\omega_0-\omega_s)-\gamma]\tau} = \frac{\mathcal{S}(t)}{\gamma - i(\omega_0-\omega_s)}. \tag{3.30}$$

The Markov approximation has been performed in Eq. 3.30, where $\tilde{\mathcal{S}}(t-\tau)$ was pulled out of the integral and approximated by its value at the current time. Here we assume that memory effects are negligible and $\mathcal{X}$ adiabatically follows the source term. This step is however only good if $\tilde{\mathcal{S}}$ varies slowly compared to the oscillatory term in the integral of Eq. 3.29. The damping constant $\gamma$ is usually included phenomenologically, assuming that the coupling to higher order correlations is well described as dephasing. It is often beneficial to consider the limiting case $\gamma \to 0$, claiming exact resonance for the interaction between system $\omega_0$ and bath $\omega_s$. In PAPER I we use this approach to obtain semi-classical Boltzmann scattering equations within a second order Born-Markov approximation for exciton-phonon correlations. In contrast, in PAPER II and III we are particularly focussing on the microscopic origin of dephasing times and their impact on optical spectra.

# 4 Excitons – Energy Quanta of the Polarization Field

In the following section the concept of excitons is introduced from a quantum field theoretical perspective. While the first part gives a short motivation for the treatment of matter-light interaction in terms of excitons, the second part introduces the bosonic approximation for pairs of electronic operators.

## 4.1 Mott-Wannier-Excitons

In this section the concept of excitons is motivated by the Coulomb-induced modification of inter-band transition energies of a semiconductor. We will later see, that the here applied basis transformation, can already be applied to the Hamiltonian, allowing to formally replace electrons and holes by excitonic operators.

### 4.1.1 Semiconductor Bloch Equations

The interaction of a semiconductor with an externally applied laser field can be described with the semi-classical Maxwell-Bloch equations. Here the macroscopic Maxwell equations are extended by a quantum mechanical description of the induced polarization field $\mathbf{P}$ in the material. While classical theories assume -per se unknown- electromagnetic response functions of the material, we can decompose the polarization $\mathbf{P}(t) = \langle \psi^\dagger \mathbf{r} \psi \rangle = \sum_{nm} \mathbf{d}_{nm} p_{nm}(t)$ into transition dipoles $\mathbf{d}_{nm} = \langle n|\mathbf{r}|m\rangle$ and quantum mechanical coherences $p_{nm} = \langle a_n^\dagger a_m \rangle$, which we will refer to as microscopic polarizations. A quantum mechanical description of the polarization field is now obtained by the Heisenberg equation of motion for the microscopic polarization. In particular, considering the Hamiltonians for electron-electron and electron light interaction and applying a Hartree-Fock factorization of Coulomb correlations, we find the semiconductor Bloch equations for the

polarization $p^{\lambda\lambda'}_{\mathbf{kk'}} = \langle a^\dagger_{\lambda\mathbf{k}} a_{\lambda'\mathbf{k'}} \rangle$ and the band occupations $f^\lambda_{\mathbf{k}} = \langle a^\dagger_{\lambda\mathbf{k}} a_{\lambda\mathbf{k}} \rangle$,

$$
\begin{aligned}
i\hbar\partial_t p^{\lambda\lambda'}_{\mathbf{kk'}} &= (\tilde{\varepsilon}^{\lambda'}_{\mathbf{k'}} - \tilde{\varepsilon}^{\lambda}_{\mathbf{k}}) p^{\lambda\lambda'}_{\mathbf{kk'}} + (f^{\lambda'}_{\mathbf{k'}} - f^{\lambda}_{\mathbf{k}}) \tilde{\Omega}^{\lambda\lambda'}_{\mathbf{kk'}}(t) && (4.1)\\
\hbar\partial_t f^\lambda_{\mathbf{k}} &= -2 \sum_{\lambda'\mathbf{k'}} \Im\mathrm{m}\{(\tilde{\Omega}^{\lambda\lambda'}_{\mathbf{kk'}})^* p^{\lambda\lambda'}_{\mathbf{kk'}}\}, && (4.2)
\end{aligned}
$$

with the Coulomb renormalized band energies,

$$
\tilde{\varepsilon}^\lambda_{\mathbf{k}} = \varepsilon^\lambda_{\mathbf{k}} - \sum_{\mathbf{q}} V^{\lambda\lambda}_{\mathbf{k},\mathbf{k+q},\mathbf{q}} f^\lambda_{\mathbf{k+q}} \tag{4.3}
$$

and the generalized Rabi energy,

$$
\tilde{\Omega}^{\lambda\lambda'}_{\mathbf{kk'}}(t) = \frac{e_0}{m_0} \mathbf{M}^{\lambda'\lambda}_{\mathbf{k}} \cdot \mathbf{A}(t) \delta_{\mathbf{kk'}} + \sum_{\mathbf{q}} V^{\lambda\lambda'}_{\mathbf{k},\mathbf{k'+q},\mathbf{q}} p^{\lambda\lambda'}_{\mathbf{k+q},\mathbf{k'+q}}. \tag{4.4}
$$

Throughout this work, we consider low excitation powers, meaning that we neglect the changes in band occupations $f$ induced by the laser pulse. Moreover, we assume that the Fermi-level lies deep within the band gap, where the latter is large compared to the considered thermal energies. In this case we can neglect the so called phase space filling, viz. $(1 - f^{\mathrm{e}}_{\mathbf{k}} - f^{\mathrm{h}}_{\mathbf{k}}) \approx 1$, as well as occupation induced energy renormalizations. For the low density regime the Bloch equations can be simplified to ($p^{cv} \to p$ and $V^{cv} \to V$):

$$
\begin{aligned}
i\hbar\partial_t p_{\mathbf{kk'}} &= -\sum_{\mathbf{q}} \mathcal{W}_{\mathbf{kk'q}} p_{\mathbf{k+q},\mathbf{k'+q}} + \frac{e_0}{m_0} \mathbf{M}^{vc}_{\mathbf{k}} \cdot \mathbf{A}(t) \delta_{\mathbf{kk'}} && (4.5)\\
\mathcal{W}_{\mathbf{kk'q}} &= \varepsilon_{\mathbf{kk'}} \delta_{\mathbf{q},0} - V_{\mathbf{k},\mathbf{k'+q},\mathbf{q}}, && (4.6)
\end{aligned}
$$

with the free particle transition energy $\varepsilon_{\mathbf{kk'}} = \varepsilon^c_{\mathbf{k}} - \varepsilon^v_{\mathbf{k'}}$. The from of Eq. 4.5 illustrates how the presence of the electron-hole interaction modifies the optical properties of the system. While in the case $V \longrightarrow 0$ the eigenfrequency of $p_{\mathbf{kk'}}$ is given by the free particle transition energy $\varepsilon_{\mathbf{kk'}}$, the presence of Coulomb interaction gives rise to a mixing of electronic states with different quasi-momenta $\mathbf{k}$, rendering it as a "bad" quantum number.

### 4.1.2 Wannier Equation

In order to obtain analytic insights into the new resonance energies of the system, we need to find the eigenvalues and -functions of the Wannier matrix

$\mathcal{W}$ on the right hand side of Eq. 4.6. Later we will perform a basis transformation to simplify the equation of motion. The corresponding eigenvalue problem reads,

$$(\varepsilon^c_{\mathbf{k}_e} - \varepsilon^v_{\mathbf{k}_h})\Phi(\mathbf{k}_e,\mathbf{k}_h) - \sum_{\mathbf{l}} V_{\mathbf{k}_e,\mathbf{k}_h+\mathbf{l},\mathbf{l}}\Phi(\mathbf{k}_e+\mathbf{l},\mathbf{k}_h+\mathbf{l}) = E^{\text{ex}}_{\mathbf{k}_e,\mathbf{k}_h}\Phi(\mathbf{k}_e,\mathbf{k}_h), \quad (4.7)$$

which resembles the Schroedinger equation for a single electron and hole, and is referred to as Wannier equation [34, 42, 44]. Here, $\Phi$ and $E^{\text{ex}}$ denote the wave function and eigenenergy of the exciton respectively. In principle Eq. 4.7 can be solved numerically when the band structure and Coulomb matrix element is known throughout the whole Brillouin zone. However, in case of so called Wannier excitons, where the binding radii are larger then the unit cell, the excitonic wave function in momentum space becomes strongly localized in the vicinity of energetic minima of the band structure. In this case the problem can be simplified significantly by expanding the bandstructure in vicinity of its extrema. Assuming that there is a local minimum in the conduction band at $\mathbf{k}_e = \mathcal{K}_e$ and a maximum of the valence band at $\mathbf{k}_h = \mathcal{K}_h$, we introduce a valley index $\zeta = (\mathcal{K}^\zeta_e,\mathcal{K}^\zeta_h)$ and decompose the momenta via $\mathbf{k}_i = \mathbf{k}^\zeta_i + \mathcal{K}^\zeta_i$. Within the valley coordinates $\mathbf{k}^\zeta_i$ the eigenvalue problem can be separated in relative ($\mathbf{q}$) and centre of mass ($\mathbf{Q}$) coordinates which are defined through the effective electron and hole valley masses $m^\zeta_e$ and $m^\zeta_h$ via

$$\mathbf{q}_\zeta = \alpha_\zeta \mathbf{k}^\zeta_h + \beta_\zeta \mathbf{k}^\zeta_e \quad \text{and} \quad \mathbf{Q}_\zeta = \mathbf{k}^\zeta_e - \mathbf{k}^\zeta_h \quad (4.8)$$

$$\mathbf{k}^\zeta_e = \mathbf{q}_\zeta + \alpha_\zeta \mathbf{Q}_\zeta \quad \text{and} \quad \mathbf{k}^\zeta_h = \mathbf{q}_\zeta - \beta_\zeta \mathbf{Q}_\zeta, \quad (4.9)$$

where $\alpha = m_e/M$,$\beta = m_h/M$ and $M = m_e + m_h$. Hence the kinetic energy of the electron hole pair can be decomposed

$$\varepsilon^c_{\mathbf{k}_e} - \varepsilon^v_{\mathbf{k}_h} = \frac{(\hbar\mathbf{k}^\zeta_e)^2}{2m^\zeta_e} + \frac{(\hbar\mathbf{k}^\zeta_h)^2}{2m^\zeta_h} + \Delta_\zeta = \frac{(\hbar\mathbf{q}_\zeta)^2}{2m^\zeta_r} + \frac{(\hbar\mathbf{Q}_\zeta)^2}{2M^\zeta} + \Delta_\zeta \quad (4.10)$$

with the reduced mass $m^{-1}_r = m^{-1}_e + m^{-1}_h$. Next we use that the electronic form factor $\mathcal{F}^\lambda_{\mathbf{k}}(\mathbf{q})$, determining the coulomb matrix element, in vicinity of band extrema can be written in terms of a phase factor $\mathcal{F}^\lambda_{\mathbf{k}}(\mathbf{q}) = \exp(i\theta^\lambda_{\mathbf{k}_\zeta} - i\theta^\lambda_{\mathbf{k}_\zeta+\mathbf{q}})$, where $\theta^\lambda_{\mathbf{k}_\zeta}$ is the topological valley phase. This phase is directly inherited by the exciton wave function, conserving important electronic selection rules. By defining a phase corrected wave function $\Psi$ via

$\Phi(\mathbf{q},\mathbf{Q}) = \exp(i\theta^e_{\mathbf{q}+\alpha\mathbf{Q}} - i\theta^h_{\mathbf{q}-\beta\mathbf{Q}})\Psi(\mathbf{q})$, we can completely split off the center-of-mass motion and find

$$\frac{(\hbar\mathbf{q})^2}{2m_r^\zeta}\Psi^{\zeta\mu}(\mathbf{q}) - \sum_{\mathbf{l}} V_\mathbf{l}\Psi^{\zeta\mu}(\mathbf{q}+\mathbf{l}) = E^\mathrm{b}_\mu\Psi^{\zeta\mu}(\mathbf{q}), \tag{4.11}$$

with the binding energy $E^\mathrm{b}_\mu$ of the excitonic state $\mu$, which is independent of the centre of mass motion. Hence, the equation of motion for the microscopic polarization can be diagonalized by performing a basis change $p_{\mathbf{k}_e,\mathbf{k}_h} \longrightarrow \pi^{\zeta\mu}_{\mathbf{Q}_\zeta}$ via

$$\begin{aligned} p_{\mathbf{k}_e,\mathbf{k}_h} &= \sum_{\zeta\mu} \pi^{\zeta\mu}_{\mathbf{Q}_\zeta}\Psi^{\zeta\mu}(\mathbf{q}_\zeta)\exp(i\theta^e_{\mathbf{q}_\zeta+\alpha_\zeta\mathbf{Q}_\zeta} - i\theta^h_{\mathbf{q}_\zeta-\beta_\zeta\mathbf{Q}_\zeta}) &(4.12)\\ &= \sum_{\zeta\mu} \pi^{\zeta\mu}_{\mathbf{k}_e-\mathbf{k}_h-\mathbf{Q}^0_\zeta}\Psi^{\zeta\mu}(\alpha_\zeta\mathbf{k}_h + \beta_\zeta\mathbf{k}_e - \mathbf{q}^0_\zeta)\exp(i\theta^e_{\mathbf{k}^\zeta_e} - i\theta^h_{\mathbf{k}^\zeta_h}) &(4.13)\end{aligned}$$

where $\mathbf{Q}^0_\zeta = \mathcal{K}^\zeta_e - \mathcal{K}^\zeta_h$ is the exciton valley and $\mathbf{q}^0_\zeta = \alpha_\zeta\mathcal{K}^\zeta_h + \beta_\zeta\mathcal{K}^\zeta_e$ is the relative momentum at which the exciton wave function is peaked. Finally, we find the equation of motion in the excitonic basis

$$\begin{aligned} i\hbar\partial_t\pi^{\zeta\mu}_\mathbf{Q} &= -E^{\zeta\mu}_\mathbf{Q}\pi^{\zeta\mu}_\mathbf{Q} + \Omega^{\zeta\mu}\delta_{\mathbf{Q},0} &(4.14)\\ E^{\zeta\mu}_\mathbf{Q} &= \frac{\hbar^2(\mathbf{Q}-\mathbf{Q}^0_\zeta)^2}{2M^\zeta} + \Delta_\zeta + E^\mathrm{b}_\mu &(4.15)\\ \Omega^{\zeta\mu} &= \frac{e_0}{m_0}\delta_{\mathcal{K}^\zeta_e,\mathcal{K}^\zeta_h}\sum_\mathbf{k}\Psi^{\zeta\mu}(\mathbf{k})^*\mathbf{M}^{vc}_\mathbf{k}\cdot\mathbf{A}(t)\exp(i\theta^e_\mathbf{k} - i\theta^h_\mathbf{k}) &(4.16)\end{aligned}$$

## 4.2 Excitonic Hamiltonian

The considerations of the last section have shown that the Coulomb interaction between electrons and holes completely restructures the eigenenergies of transitions between conduction and valence band. We found that the expansion of inter-band transition amplitudes $p_{k_e,k_h}$ can be drastically simplified by expanding them in terms of excitonic wave functions. In principle, this basis transformation can also be done in other equations of motion, e.g. those involving phonon-scattering and higher order electron hole correlations, which are important for the luminescence of the system. However, the derivation of Coulomb contributions to the equations of motion in the electron-hole

picture are often quite cumbersome and the exciton basis transformation also becomes more complex when dealing with e.g. two-particle correlations. Therefore it is convenient to apply the Hartree-Fock approximation and low-excitation limit directly on the level of the Hamiltonian and transform the electron-hole operators into exciton basis. This step dramatically simplifies the derivation of equations of motion and allows to study higher order processes such as phonon-assisted exciton-photon interaction thanks to a reduced number of operators in play. While the transformation procedure shown below has a rather empirical character, the resulting Hamiltonian hast the same form as obtained in more sophisticated theoretical approaches towards excitonic Hamiltonians [51–53].

The first step towards an excitonic Hamiltonian is the definition of electron-hole-pair operators $A$ as combination of conduction ($c$) and valence band ($v$) electrons:

$$A^\dagger_{\mathbf{k}\mathbf{k}'} = c^\dagger_{\mathbf{k}} v_{\mathbf{k}'} \tag{4.17}$$

$$\begin{aligned}[A_{\mathbf{k}_1\mathbf{k}_2}, A^\dagger_{\mathbf{k}_3\mathbf{k}_4}] &= \delta_{\mathbf{k}_1\mathbf{k}_3}\delta_{\mathbf{k}_2\mathbf{k}_4} - \chi_{\mathbf{k}_1\mathbf{k}_2\mathbf{k}_3\mathbf{k}_4} \\ &\approx \delta_{\mathbf{k}_1\mathbf{k}_3}\delta_{\mathbf{k}_2\mathbf{k}_4}\end{aligned} \tag{4.18}$$

Here the term $\chi_{1234} = v_4 v_2^\dagger \delta_{13} + c_3^\dagger c_1 \delta_{24}$ accounts for the fermionic substructure of the otherwise bosonic pair operators. Since $\chi$ resembles the operator for the electron and hole densities, in the low excitation limit, we can set $\langle\chi\rangle << 1$, giving rise to a fully bosonic commutation of electron-hole excitations. In order to describe the full Hamiltonian in terms of pair creation operators, we now need to find a way to express intra-band transitions, such as $c_1^\dagger c_2$, as combinations of inter-band operators $A$. Since the many-particle dynamics of the system is fully determined by the commutator with the Hamiltonian, we can change the representing operators when conserving the underlying commutation relations. As an example, we consider the follwing equivalent commutators

$$[c_1^\dagger c_2, A_{34}^\dagger] = [c_1^\dagger c_2, c_3^\dagger v_4] = c_1^\dagger v_4 \delta_{23} = A_{14}^\dagger \delta_{23} = \sum_i [A_{1i}^\dagger A_{2i}, A_{34}^\dagger]. \tag{4.19}$$

Similar relations can be shown for $A$ and/or intra-band transitions in the valence band. Consequently, when strictly neglecting the correction factors

$\chi$, the following substitutions are valid in the Hamiltonian:

$$c^\dagger_{\mathbf{k}} c_{\mathbf{k}'} \quad \longrightarrow \quad \sum_{\mathbf{l}} A^\dagger_{\mathbf{kl}} A_{\mathbf{k}'\mathbf{l}} \tag{4.20}$$

$$v_{\mathbf{k}} v^\dagger_{\mathbf{k}'} \quad \longrightarrow \quad \sum_{\mathbf{l}} A^\dagger_{\mathbf{lk}} A_{\mathbf{lk}'} \tag{4.21}$$

Next we neglect the intra-band Coulomb interaction, which for higher densities gives rise to band gap renormalization and electron-electron scattering, but in the low excitation regime has no impact on the dynamics of the system on a Hartree-Fock level. Hence the electronic part of the Hamiltonian can be rewritten as:

$$H_{\text{el}} \rightarrow H_{\text{x-0}} = \sum_{\mathbf{k}\mathbf{k}'} \left[ (\varepsilon^c_{\mathbf{k}} - \varepsilon^v_{\mathbf{k}'}) A^\dagger_{\mathbf{k}\mathbf{k}'} - \sum_{\mathbf{q}} V_{\mathbf{k}\mathbf{k}'\mathbf{q}} A^\dagger_{\mathbf{k}+\mathbf{q},\mathbf{k}'+\mathbf{q}} \right] A_{\mathbf{k}\mathbf{k}'} \tag{4.22}$$

$$= \sum_{\zeta\mu\mathbf{Q}} E^{\zeta\mu}_{\mathbf{Q}} X^\dagger_{\zeta\mu\mathbf{Q}} X_{\zeta\mu\mathbf{Q}}, \tag{4.23}$$

where in the last line we used the expansion into excitonic eigenmodes,

$$A^\dagger_{\mathbf{k}_e\mathbf{k}_h} = \sum_{\zeta\mu} X^\dagger_{\zeta\mu,\mathbf{k}_e-\mathbf{k}_h-\mathbf{Q}^0_\zeta} \Psi^{\zeta\mu}(\alpha_\zeta \mathbf{k}_h + \beta_\zeta \mathbf{k}_e - \mathbf{q}^0_\zeta) \exp(i\theta^e_{\mathbf{k}^\zeta_e} - i\theta^h_{\mathbf{k}^\zeta_h}) \tag{4.24}$$

which is analogue to the transformation of the microscopic polarization Eq.4.12. Note that the Coulomb interaction is now fully contained within the exciton single particle energy. In the electron picture the Hamiltonian contained many-particle interactions, giving rise to a hierarchy problem in Coulomb correlations. Now the negligence of the fermionic correction term $\chi$ has led to an effective single particle problem. With the above described transformation and commutation rules, we have restricted the problem to the low density regime and applied a Hartree-Fock factorization of the Coulomb interaction directly within the Hamiltonian.

Applying the same approach to the electron-phonon scattering gives rise to a convenient exciton-phonon Hamiltonian:

$$H_{\text{x-ph}} = \sum_{\zeta\mu\rho\nu,\mathbf{q}\mathbf{Q}} D^{\rho\nu,\zeta\mu}_{\mathbf{Q}\mathbf{q}} X^\dagger_{\zeta\mu,\mathbf{Q}+\mathbf{q}} X_{\rho\nu,\mathbf{Q}} (b_{\mathbf{q}} + b^\dagger_{\mathbf{q}}) \tag{4.25}$$

Interestingly, the Hamiltonian above has the same form as the electron-phonon scattering. However the exciton-phonon matrix $D$ now has two contributions stemming from scattering of electrons and holes respectively:

$$
\begin{aligned}
D^{\rho\nu,\zeta\mu}_{\mathbf{Qq}} &= (D^{\rho\nu,\zeta\mu}_{\mathbf{Qq}})^c - (D^{\rho\nu,\zeta\mu}_{\mathbf{Qq}})^v && (4.26)\\
(D^{\rho\nu,\zeta\mu}_{\mathbf{Qq}})^c &= \delta_{\mathcal{K}^\rho_h,\mathcal{K}^\zeta_h}\tilde{D}^c_{\mathcal{K}^\rho_e\to\mathcal{K}^\zeta_e,\mathbf{q}}\sum_{\mathbf{k}}\Psi^{\rho\nu *}(\mathbf{k})\Psi^{\zeta\mu}(\mathbf{k}+\beta_\zeta\Delta\mathbf{k}^{\rho\zeta}_e[\mathbf{q},\mathbf{Q}]) && (4.27)\\
(D^{\rho\nu,\zeta\mu}_{\mathbf{Qq}})^v &= \delta_{\mathcal{K}^\rho_e,\mathcal{K}^\zeta_e}\tilde{D}^v_{\mathcal{K}^\rho_h\to\mathcal{K}^\zeta_h,\mathbf{q}}\sum_{\mathbf{k}}\Psi^{\rho\nu *}(\mathbf{k})\Psi^{\zeta\mu}(\mathbf{k}-\alpha_\zeta\Delta\mathbf{k}^{\rho\zeta}_h[\mathbf{q},\mathbf{Q}]) && (4.28)\\
\Delta\mathbf{k}^{\rho\zeta}_i[\mathbf{q},\mathbf{Q}] &= \mathbf{q}-\mathcal{K}^\rho_i+\mathcal{K}^\zeta_i+(1-\frac{M_\zeta}{M_\rho})\mathbf{Q} && (4.29)
\end{aligned}
$$

The appearing overlap of excitonic wave functions $\sum_k \Psi_i(k)\Psi_j(k+p)$ is the momentum space representation of the scattering form factor $\mathcal{F}_{ij}(p) = \langle i|e^{ipr}|j\rangle$, which is a probability measure of the transition $i \to j$ under momentum transfer $p$. In the case of intra-valley scattering ($\zeta = \rho$) we find that the exciton-phonon matrix element $D^{ij}_q \propto D^c_q\mathcal{F}_{ij}(\beta q) - D^v_q\mathcal{F}_{ij}(-\alpha q)$. This reflects the fact that the exciton can change its centre of mass momentum by $q$, either by electron-phonon scattering in the conduction band, which is accompanied with a change of the relative momentum by $\beta q$, or in the valence band (hole scattering), which simultaneously transfers the relative momentum $-\alpha q$. Hence the excitonic form factors account for the simultaneous transfer of relative momentum when the exciton changes its centre of mass momentum, which can be interpreted as exciton-phonon selection rules.

Finally, the exciton-photon interaction is also transformed giving rise to

$$
\begin{aligned}
H_{x-pt} &= \sum_{\sigma\mathbf{q},\zeta\mu} g^{\zeta\mu}_{\sigma\mathbf{q}} X^\dagger_{\zeta\mu,0} B_{\sigma\mathbf{q}} + h.a. && (4.30)\\
g^{\zeta\mu}_{\sigma\mathbf{q}} &= \delta_{\mathbf{q}_\parallel,0}\delta_{\mathcal{K}^\zeta_e,\mathcal{K}^\zeta_h}\tilde{g}^{cv}_{\sigma\mathbf{q}}\sum_{\mathbf{k}}\Psi^{\zeta\mu}(\mathbf{k}). && (4.31)
\end{aligned}
$$

In contrast to the other Hamiltonians above, the exciton-photon interaction describes a conversion of excitons to photons and vice versa, which does not conserve the total number of excitons. The excitonic factor $\sum_k \Psi(k) = \tilde{\Psi}(r=0)$, reflects the fact that excitons can only recombine if the probability of finding an electron and hole at the same position is not zero (as e.g. for p-type wave functions). Note that the electronic matrix elements appearing

in the exciton-photon/phonon matrix are phase free (symbolized by $\tilde{g}$ and $\tilde{D}$), since the electronic valley phases exactly cancel with the exciton phase, as explicitly shown for the optical matrix element in the last section.

In the following sections, the valley index will be suppressed or rather included within the exciton compound index. Moreover, the weak $\mathbf{Q}$ dependence of the exciton-phonon matrix element is neglected to simplify the numerical treatment of scattering equations.

# 5 Exciton Spectroscopy

In the following section we review the experimental observables studied in this work. Hereby, we focus on how different emission and absorption spectra can be related to exciton properties of the system. The actual results of this thesis, e.g. calculated spectra and their comparison to the experiment, are discussed in the next section.

## 5.1 Linear Absorption – Probing Interband Transitions

One of the standard techniques to characterize the properties of a material is the absorption or transmission spectroscopy. Here the laser field transmission through / reflection from the sample is measured in dependence of the wavelength to determine the resonance energies of the material. The absorption coefficient $\alpha \propto \Im\mathrm{m}\{\chi\}$ is given by the electromagnetic susceptibility $\chi$, which describes the relationship between the incident light field $\mathbf{E}$ and the induced polarization $\mathbf{P}$ of the material. For weak excitation conditions it holds,

$$P_i(\omega) = \epsilon_0 \sum_j \chi_{ij}^{(1)}(\omega) E_j(\omega) \tag{5.1}$$

$$\chi_i(\omega) = \frac{P_i(\omega)}{\epsilon_0 E_i(\omega)} = \frac{j_i(\omega)}{\epsilon_0 \omega^2 A_i(\omega)} \qquad (\text{for} \quad \chi_{ij}^{(1)} = \chi_i \delta_{ij}) \tag{5.2}$$

In the second step we have expressed the electrical field in terms of the vector potential and rewrite the oscillating polarization as a macroscopic current $\mathbf{j} = \partial_t \mathbf{P}$. To calculate the response $\chi$ in a quantum mechanical frame work, the current $j$ is interpreted as the probability current [33]

$$\langle \mathbf{j} \rangle = \frac{e_0}{m_0 V} \int d^3r \langle \Psi^\dagger(\mathbf{r}) \mathbf{p} \Psi(\mathbf{r}) \rangle \tag{5.3}$$

$$\Rightarrow \langle \mathbf{j} \rangle \big|_{\text{inter}} = \frac{2e_0}{m_0 V} \sum_{\mathbf{k}} \Re\mathrm{e}\{\mathbf{M}_{\mathbf{k}}^{vc*} p_{\mathbf{k}}^{cv}\} \tag{5.4}$$

Note that we here only took into account the contribution resulting from interband transitions, since absorption experiments are usually performed in

frequency ranges, which are to large to induce oscillations of charge carrier occupations (cf. Sec. 5.2). To determine how the polarization reacts to the incident light field, we make use of the semiconductor Bloch equations for the microscopic polarization $p^{cv}$, cf. Sec. 4. The transformation into exciton basis and evaluation of the Bloch equations in frequency domain gives rise to the Elliot formula for the excitonic absorption [42, 54, 55],

$$\alpha_\sigma(\omega) = \frac{e_0^2}{m_0^2 \epsilon_0 n c_0 \omega} |M_\sigma^{vc}|^2 \sum_\mu \Im\mathrm{m}\Big( \frac{|\sum_{\mathbf{k}} \Psi_\mu(\mathbf{k})|^2}{E_0^\mu - \hbar\omega - i\Gamma_\mu} \Big) \delta_{\mathcal{K}_e^\mu, \mathcal{K}_h^\mu}. \tag{5.5}$$

Hence, each momentum direct excitonic state $\mu$ contributes a Lorentzian response at its eigenenergy $E_0^\mu$. The peak surface (oscillator strength) is given by the probability to find the electron and hole at the same position $\tilde{\Psi}_\mu(\mathbf{r} = 0) = \sum_{\mathbf{k}} \Psi_\mu(\mathbf{k})$. The width of the peaks is determined by the parameter $\Gamma$ containing all mechanisms leading to a decay of the polarization. In PAPER II we have used a second order Born Markov approximation for exciton-phonon $\langle X_\mu^\dagger b^{(\dagger)} \rangle$ and exciton-photon correlations $\langle X_\mu^\dagger B^{(\dagger)} \rangle$ to calculate the scattering induced broadening of exciton resonances, which will be discussed in Sec. 6.

Note that the above equation only holds for weak excitation conditions, since we assume negligible electron and hole densities. For intermediate and high excitation powers, the phase space filling factors in the Bloch equation become dominant giving rise to a so called absorption bleaching. Moreover, significant amounts of excited electrons and holes lead to changes in the exciton binding energy (blue shift), band gap renormalizations (red shifts) [56–58].

## 5.2 Pump-Probe – Mapping Internal Transitions

In contrast to linear absorption experiments, addressing the static properties of the system, the so called pump-probe spectroscopy allows to study the dynamics of excited charge carriers and - similarly intriguing- the internal degrees of freedom of excited quasi-particles. The most frequently used pump-probe method uses two pulses adressing interband transitions. While the first pump pulse is strongly absorbed by the material, giving rise to excited charge carriers in the conduction band, the second probe pulse becomes

less absorbed by the material, which results from the Pauli blocking of the already excited carriers. Therefore, the change in the absorbtion of the probe pulse as function of delay between pump and probe provides information of the carrier relaxation process on ultrafast timescales. However, in this thesis we focus on a slightly different approach to pump-probe spectroscopy, where the probe pulse adresses low frequency intraband transitions. The idea behind this technique is that the presence of excitons created by the first pump pulse can significantly modify the low frequency response of the material, which subsequently can be probed by the absorbtion of a the probe pulse [59, 60]. The reason for the change in the response function, is that the optically injected excitons can interact with light by performing transitions between internal degrees of freedom, e.g. from their ground state (1s) to the first excited state (2p). For TMD monolayers, this change in the relative motion of the electron-hole pair can occur via the absorption of terahertz/far infra-red light [21, 61, 62]. From a theoretical point of view, the so called intra-excitonic response results from oscillating intraband currents induced by the electrical field of the probing laser. To derive the response function we consider the intraband contribution of the electron-light interaction [63, 64]

$$H_{\text{intra}} = \sum_{\lambda\mathbf{k}} \mathbf{j}^{\lambda}_{\mathbf{k}} \cdot \mathbf{A} a^{\dagger}_{\lambda\mathbf{k}} a_{\lambda\mathbf{k}}; \qquad \mathbf{j}^{\lambda}_{\mathbf{k}} = \frac{e_0}{\hbar} \nabla_{\mathbf{k}} \varepsilon^{\lambda}_{\mathbf{k}} \tag{5.6}$$

as well as the intraband contribution to the quantum mechanical current,

$$\langle \mathbf{j} \rangle \big|_{\text{intra}} = \sum_{\lambda\mathbf{k}} \mathbf{j}^{\lambda}_{\mathbf{k}} f^{\lambda}_{\mathbf{k}}. \tag{5.7}$$

While the intraband current results from asymmetries in the electronic occupation, the intraband Hamiltonian Eq. 5.6 corresponds to an oscillation of the electronic bandstructure, which does not directly influence the carrier occupation dynamics, viz. $[a^{\dagger}_i a_i, H_{\text{intra}}] = 0$. However, the carrier occupations are coupled to intra-excitonic correlations through the Coulomb interaction ( $\partial_t f_i \propto V \langle X^{\dagger}_{\nu} X_{\mu} \rangle$ with $\mu \neq \nu$). These excitonic correlations in turn do couple to the low frequency fields, since they induce periodic changes of the band gap. Consequently, transitions between different exciton states also lead to a reconfiguration of the electron-hole occupation and thus potentially to a current. Evaluating the equation of motion for the transition correlations $\langle X^{\dagger}_{\nu} X_{\mu} \rangle$ in the frequency domain yields the atom-like Elliot response [63, 65]

$$\chi_{\sigma}(\omega) \big|_{\text{intra}} \propto \frac{1}{\omega^2} \sum_{\nu\mu\mathbf{Q}} \frac{|j^{\nu\mu}_{\sigma}|^2 (N^{\nu}_{\mathbf{Q}} - N^{\mu}_{\mathbf{Q}})}{E^{\nu}_{\mathbf{Q}} - E^{\mu}_{\mathbf{Q}} - \hbar\omega - i(\Gamma^{\nu}_{\mathbf{Q}} + \Gamma^{\nu}_{\mathbf{Q}})} \tag{5.8}$$

where $N^{\nu}_{\mathbf{Q}} = \langle X^{\dagger}_{\nu\mathbf{Q}} X_{\nu\mathbf{Q}} \rangle$ is the exciton density. Again we find a sum of lorentzian responses, however here at energies corresponding to intra-exciton transitions. From the form of the excitonic current matrix element

$$j^{\nu\mu}_{\sigma(\mathbf{Q})} = \hat{\mathbf{e}}_{\sigma} \sum_{\mathbf{k}} \Psi^{*}_{\nu}(\mathbf{k}) \Psi_{\mu}(\mathbf{k}) (\mathbf{j}^{c}_{\mathbf{k}+\alpha\mathbf{Q}} - \mathbf{j}^{c}_{\mathbf{k}+\beta\mathbf{Q}}) \delta_{\zeta_{\mu},\zeta_{\nu}} \tag{5.9}$$

$$= \hat{\mathbf{e}}_{\sigma} \frac{e\hbar}{m_r} \sum_{\mathbf{k}} \mathbf{k} \Psi^{*}_{\nu}(\mathbf{k}) \Psi_{\mu}(\mathbf{k}) \delta_{\zeta_{\mu},\zeta_{\nu}}, \tag{5.10}$$

we can directly read off important optical selection rules. Only when the product of initial and final state is antisymmetric, the transition is optically allowed. For the radially symmetric problem this means that the angular quantum number has to change by one, just as in atomic transitions. In contrast to the linear absorption, the intra-excitonic response is proportional to the exciton number, since the bare semiconductor does not share the resonance energies of the quasi-particles it can host. Therefore, the low frequency response after an initial laser excitation can not only be used to map intra excitonic transition energies, but also provides access to the time dependent exciton distribution.

## 5.3 Photoluminescence - Traces of Recombinations

An other complementary experimental technique to the absorption spectroscopy is the detection of the delayed light emission stemming from the material after an initial excitation, which is referred to as photoluminescence (PL). While the absorption spectrum reveals the frequencies at which the system responds to a coherent excitation, the PL spectrum represents a finger print of the incoherent emission stemming from the spontaneous recombination of electron hole pairs. One of the advantages of this technique is that the signal, similar as in the case of pump-probe, is proportional to the occupation probability of the initial states [66]. Therefore, the low temperature emission can reveal quantum states with very weak matter-light coupling, only becoming visible due to large occupations. From a theoretical point of view, the measured PL intensity is proportional to the energy flux $\mathbf{S}$ of the electromagnetic field, which obeys the continuity equation

$$\nabla \cdot \mathbf{S} = -\partial_t \rho_{\mathrm{EM}} \tag{5.11}$$

Assuming that the detector integrates over an infinitely large sphere, we can use Gauss law to obtain the radiation power

$$P_{\text{rad}} = \oint \mathbf{dA}\cdot\mathbf{S} = \partial_t \int d^3r \frac{1}{2}(\varepsilon_0 \mathbf{E}^2 + \frac{1}{\mu_0}\mathbf{B}^2) \tag{5.12}$$

$$= \sum_{\sigma\mathbf{q}} \hbar\omega_{\mathbf{q}} \partial_t \langle B^\dagger_{\sigma\mathbf{q}} B_{\sigma\mathbf{q}}\rangle = \int d\omega \hbar\omega I(\omega,t). \tag{5.13}$$

In the second line we have used the expansion of the electromagnetic field in terms of photon creation and annihilation operators, cf. Sec. 3, and introduced a spectral decomposition of the radiation power, defining the spectral PL signal (photon flux)

$$I(\omega,t) = \sum_{\sigma\mathbf{q}} \dot{n}_{\sigma\mathbf{q}}(t)\delta(\omega-\omega_{\mathbf{q}}) \tag{5.14}$$

as a measure for the temporal change of the photon number $n_{\mathbf{q}} = \langle B^\dagger_{\mathbf{q}} B_{\mathbf{q}}\rangle$. Hence, to calculate the emission spectrum of a material, we have to solve the equation of motion of the photon numbers, which are coupled to the excitonic system via the photon-assisted polarization $S^\mu_{\mathbf{q}} = \langle B^\dagger_{\mathbf{q}} X_\mu\rangle$. Here different orders of many-particle correlations within the hierarchy of exciton-photon/phonon correlations, give rise to a variety of intriguing spectral phenomena within the PL. In particular, the form of the exciton-photon interaction Hamiltonian cf. Sec. 3, illustrates that each creation of a photon is accompanied by the annihilation of an exciton. Hence, the spectrally and temporally resolved PL spectrum can provide information about the energy as well as occupation dynamics of different exciton species. In PAPER III we have investigated the impact of phonon-assisted recombinations of momentum-indirect dark excitons on the PL spectrum, which is also outlined in Sec. 6.

# 6 Results

In this section we summarize the main results of this thesis. Based on the theoretical approach presented in the previous sections, we have studied different aspects of the exciton-phonon and exciton-photon interaction including linear optical properties, formation of bound excitons out of a free electron-hole gas as well as the phonon-assisted radiative decay of dark excitons. While several aspects of these properties/phenomena have already been studied in previous works [29, 30, 32, 67], the special focus of this work is to investigate the impact of excited exciton states (Rydberg excitons) as well as the influence of indirect excitons, where electrons and holes are located at different high symmetry points of the Brillouin zone.

## 6.1 Linewidth of Exciton Resonances

While conventional semiconductor systems used to study exciton properties, e.g. GaAs quantum wells, usually only exhibit one distinguishable exciton resonance, the significantly increased Coulomb interaction in TMDs and the related increase in exciton binding energies allows to spectrally resolve several excited excitons between ground state and band edge. In particular the rather new method of encapsulating monolayers with hexagonal boron nitride (hBN) reduces the inhomogeneous broadening of spectral lines, making the intrinsic linewidth of excitons accessible. The position of excitonic resonances in the absorption spectrum provides information about the binding energies and thus the Coulomb forces in the system [16, 68]. In addition to that, the linewidth is a measure for the lifetime of the induced optical coherences and therefore contains information about the many-particle scattering processes [29, 69–73]. In particular, the broadening $\Gamma_\mu$ in the low excitation regime, cf. Eq. 5.5 results from the interaction between excitons and phonons or photons $\Gamma_\mu = \Gamma_\mu^{\text{rad}} + \Gamma_\mu^{\text{phon}}$. To obtain access to these dephasing rates, we solve the equations of motion for exciton-phonon $\langle A_\mu^\dagger b^{(\dagger)} \rangle$ and exciton-photon correlations $\langle A_\mu^\dagger B^{(\dagger)} \rangle$ within a Born-Markov approximation [29, 74, 75], which

gives rise to the Fermi golden rules,

$$\Gamma_\mu^{\rm rad} = \pi \sum_{\sigma \mathbf{q}_\perp} |g^\mu_{\sigma \mathbf{q}_\perp, 0}|^2 \delta(E_0^\mu - \hbar\omega_{\mathbf{q}_\perp}) \tag{6.1}$$

$$= \frac{\hbar e_0^2}{2m_0^2 \epsilon_0 n c_0} \sum_\sigma |M_\sigma^{vc}|^2 \frac{|\sum_{\mathbf{k}} \Psi_\mu(\mathbf{k})|^2}{E_0^\mu} \tag{6.2}$$

$$\Gamma_\mu^{\rm phon} = \pi \sum_{\pm,\lambda,\nu,\mathbf{q}} |D^{\mu\nu}_{\lambda\mathbf{q}}|^2 (\frac{1}{2} \pm \frac{1}{2} + n_{\lambda\mathbf{q}}) \delta(E^\nu_{\mathbf{q}} - E_0^\mu \pm \hbar\Omega_{\lambda\mathbf{q}}). \tag{6.3}$$

Figure 3(a) schematically illustrates the exciton bandstructure and relevant scattering mechanisms. Excitons are excited at zero center-of-mass momentum and can either decay by radiative recombination (yellow) or scatter into a dark state with a non-zero center-of-mass momentum. Apart from intravalley scattering via absorption of -mostly low energy acoustic- phonons (orange) or transitions into lower lying states after emission of a phonon (red), the electron or hole can scatter into a different valley (blue) giving rise to indirect intervalley excitons.

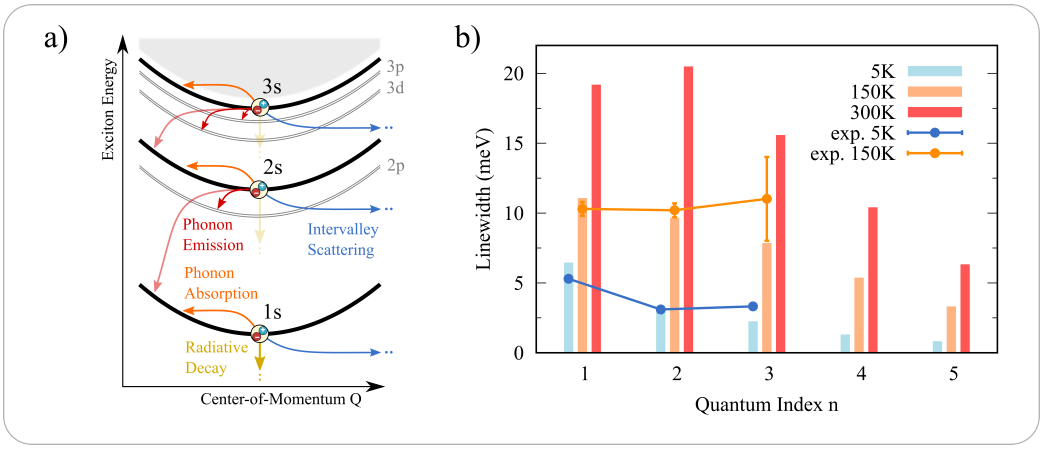


Figure 3: Exciton dephasing mechanisms. a) Schematic illustration of the exciton bandstructure and possible scattering mechanisms. Radiative recombination or scattering into a dark state with finite center-of-mass momentum via interaction with phonons leads to a broadening of exciton absorption lines. b) The linewidth of bright ns excitons as function of n for dfferent temperatures. Our microscopic model yields a decreasing trend for high n resulting from a reduced scattering efficiency for excited states.

Fig. 3 (b) shows the calculated full width at half maximum of exciton absorption lines (s-type states) calculated with Eq. 6.2 and 6.3 as a function of the principal quantum number n for three different temperatures. The calculated values are based on parameters for $WSe_2$ encapsulated with hBN [23, 40, 49, 76] (represented as bars) and are directly compared to the experimentally measured values (points). Apart from the case of the 2s exciton at room temperature, we find – in reasonable agreement with the experiment – a general decrease of the linewidth with increasing quantum index n. This result somehow contradicts the physical intuition, since excited states have a larger phase space of lower lying states to scatter into. To understand the observed behaviour we have to consider the influence of exciton wave functions on radiative and non-radiative scattering probabilities. With increasing index n the orbital functions become larger in space, which reduces the radiative recombination efficiency $\propto \tilde{\Psi}(\mathbf{r} = 0)$ , cf. Eq.6.2. At the same time the larger orbitals of excited states correspond to narrower wave functions in momentum space. Since the exciton-phonon matrix element is given by the overlap of initial and final state in momentum space, cf. Eq. 4.28, larger exciton radii lead to a reduction of scattering probabilities [51, 77, 78]. This is similar to Heisenbergs uncertainty principle, in the sense that a weaker localization in space yields smaller momentum uncertainties and therefore a reduced tolerance for momentum transfers. In PAPER II we analyse the temperature dependence of different contributions to the linewidth and discuss in detail the comparison between experiment and theory. The overall good comparison between the theoretically predicted intrinsic scattering rates and the actually measured broadening indicates that the studied hBN encapsulated samples are only weakly influenced by inhomogeneities, which is further elaborated on in PAPER XIII. Moreover, in PAPER XV we ivestigated the impact of elastic impurity scattering on the linewidth of different exciton states. Here we find similar behaviour with increasing quantum index as observed for scattering with phonons. However, due to the lack of resonant states, the elastic scattering with impurities is strongly suppressed in the ground state, while phonon-scattering is very efficient.

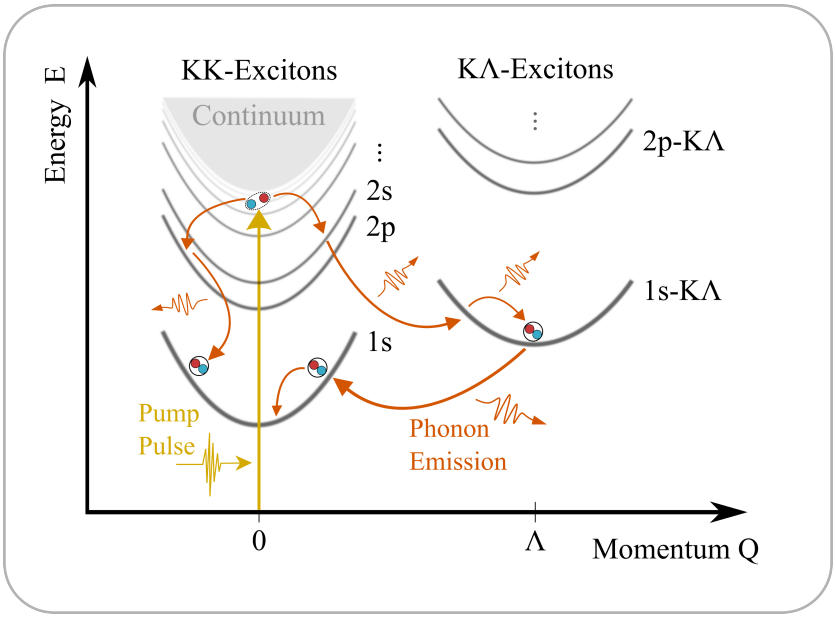


Figure 4: Intra-excitonic relaxation cascade in $MoSe_2$. Excited hot electron-hole pairs dissipate energy via a sequence of phonon emissions, performing a cascade-like relaxation through the Rydberg series of exciton states including momentum indirect KΛ states. Figure is also published in PAPER I under the Creative Commons Attribution 4.0 International License, cf. https://creativecommons.org/licenses/by/4.0/.

## 6.2 Exciton Relaxation Cascade

TMD monolayers are considered as promising candidates for the realization of atomically thin solar cells, photo detectors and other optoelectronic semiconductor devises. However, most of these devices conceptionally require freely moving charge carriers. However, since excitons represent bound electron-holes states, which are externally charge neutral, they give rise to much different conductivity properties then free charges. Therefore a technological application of these materials requires a microscopic understanding of the formation of bound excitons out of a quasi-free electron-hole plasma. Within our theoretical approach we can derive the phonon-induces relaxation dynamics of coherent excitonic polarizations $P^{\mu}_{\mathbf{Q}} = \langle X^{\dagger}_{\mu\mathbf{Q}} \rangle$ as well as incoherent exciton occupations $N^{\mu}_{\mathbf{Q}} = \langle X^{\dagger}_{\mu\mathbf{Q}} X_{\mu\mathbf{Q}} \rangle - |P^{\mu}_{\mathbf{Q}}|^2$. Again we treat exciton-phonon and exciton-photon correlations within a second order Born Markov

approximation giving rise to the coupled equations of motion [29, 32, 75]

$$\dot{P}^{\mu} = \frac{i}{\hbar}\left(E_0^{\mu} + i\Gamma_{\mu}^{\mathrm{rad}} + \frac{i\hbar}{2}\sum_{\nu\mathbf{Q}}\sigma_{\mathbf{0Q}}^{\mu\nu}\right)P^{\mu} + i\Omega^{\mu}, \tag{6.4}$$

$$\dot{N}_{\mathbf{Q}}^{\mu} = \sum_{\nu}\sigma_{\mathbf{0Q}}^{\nu\mu}|P^{\nu}|^2 - \frac{2}{\hbar}\Gamma_{\mu}^{\mathrm{rad}}\delta_{\mathbf{Q},\mathbf{0}}N_{\mathbf{Q}}^{\mu} + \sum_{\nu\mathbf{Q}'}(\sigma_{\mathbf{Q}'\mathbf{Q}}^{\nu\mu}N_{\mathbf{Q}'}^{\nu} - \sigma_{\mathbf{QQ}'}^{\mu\nu}N_{\mathbf{Q}}^{\mu}), \tag{6.5}$$

$$\sigma_{\mathbf{QQ}'}^{\mu\nu} = \frac{2\pi}{\hbar}\sum_{\pm,\lambda}|D_{\lambda,\mathbf{Q}-\mathbf{Q}'}^{\mu\nu}|^2\left(\frac{1}{2} \pm \frac{1}{2} + n_{\mathbf{Q}-\mathbf{Q}'}^{\lambda}\right)\delta(E_{\mathbf{Q}'}^{\nu} - E_{\mathbf{Q}}^{\mu} \pm \hbar\omega_{\mathbf{Q}-\mathbf{Q}'}^{\lambda}) \tag{6.6}$$

where $\sigma_{\mathbf{QQ}'}^{\mu\nu}$ is the probability to scatter from state ($\mu$,$\mathbf{Q}$) to ($\nu$,$\mathbf{Q}'$). Note, that the solutions of the Wannier equation (index $\mu$) contain bound electron-hole pairs (negative eigenenergy), but also a continuum of free scattering states (positive eigenenergy) which resemble the free electron and hole plasma states with pair energies above the band edge.

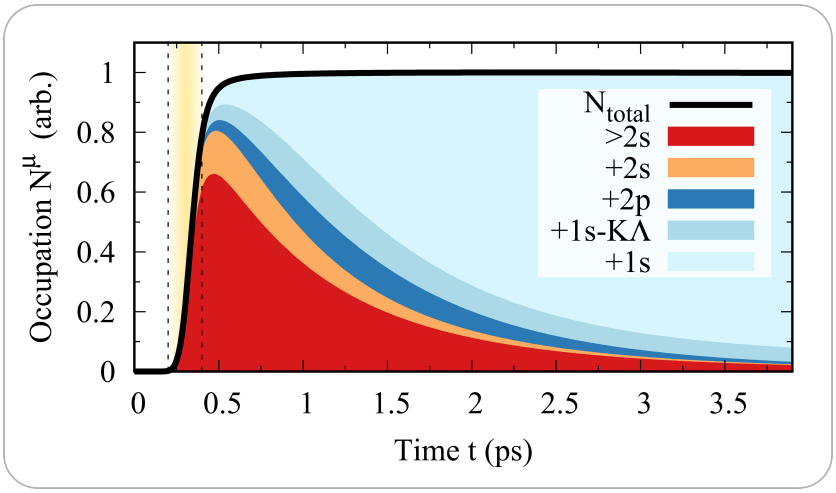


Figure 5: Exciton formation and relaxation dynamics. Evolution of the momentum integrated exciton occupations N. The black line shows the overall number of incoherent excitons, while the coloured surfaces below the black line represent the relative fraction of the respective exciton state. After 1.5 ps a 1/e-fraction of the excited pairs has relaxed into the 1s-ground state. Figure is also published in PAPER I under the Creative Commons Attribution 4.0 International License, cf. https://creativecommons.org/licenses/by/4.0/.

Figure 4 schematically illustrates the exciton band structure and the dominant relaxation mechanisms after an excitation close to the band edge. The

pump pulse creates quasi-free electron-hole pairs at the scattering continuum (yellow arrow), which subsequently dissipate their excess energy via a sequence of phonon emissions, performing a cascadic relaxation [79] across the Rydberg-series of lower lying exciton states (orange arrows), in particular also scattering to momentum indirect pairs, such as KΛ excitons. Fig. 5, shows the simulated exciton dynamics after an excitation 20 meV below the free-particle band gap and parameters for $MoSe_2$ on a $SiO_2$ substrate. The colour-coded areas under the black curve (total number of electron-hole pairs) illustrate the fractions of appearing exciton states. Note that the contributions were added up successively to pile up to the total number. Moreover, the large amount of different excited states close to the band gap ($E > E_{2s}$) have been grouped for a better overview. After the optical excitation (yellow shaded area) most electron-hole pairs occupy exciton states above the 2s. Those hot pairs dissipate their energy by decaying into lower lying states via the emission of phonons. Our simulation predicts that after 1.5 ps a 1/e-fraction of the excited pairs has decayed into the 1s-ground state revealing an ultrafast formation of bound excitons out of a free electron-hole plasma. In PAPER I we discuss the most efficient relaxation channels determined by the symmetries of exciton wave functions and the arrangement of energy levels. Moreover, we also show snap shots of the momentum resolved exciton dynamics across the Rydberg series of bright and dark exciton states.

As discussed in Sec. 5, ultrafast pump-probe experiments can be utilized to make the exciton dynamics experimentally accessible. Probing intra-excitonic transition after an interband pump pulse allows to indirectly measure the relaxation dynamics on a femtosecond timescale, since the response is proportional to the occupation of the states involved in the transition. Figure6 shows the calculated low frequency absorption as function of the probe energy at different delay times after the pump. The colour shaded curves result from the dynamics at room temperature, while the black curves show the resulting spectra simulated for 77 K. Shortly after the pump pulse (t=0.5 ps and t=1 ps) we predict several absorption peaks at low energies, predominantly stemming from the close lying transitions of high energy excitons. In particular, we predict that transient population inversions between s- and p-states arise during the relaxation process, since the relaxation preferably occurs between states with the same orbital symmetry. For the spectra measured at 77 K, where the absorption lines become narrow enough, we therefore observe pronounced gain signals (i.e. negative absorption).With

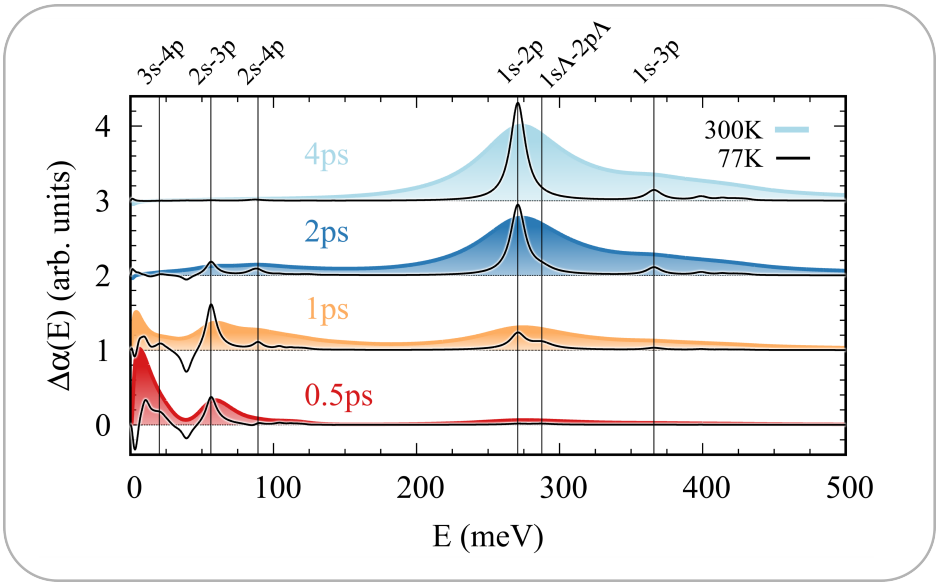


Figure 6: Pump-induced low frequency absorption as function of the probe energy for four different times. Shortly after the pump the occupation of excited states leads to multiple absorption features for energies below 150 meV, inter alia optical gain resulting from transient population inversions. For large delay times the spectrum is dominated by the response of the 1s-2p transitions of excitons in the ground state. Figure is also published in PAPER I under the Creative Commons Attribution 4.0 International License, cf. https://creativecommons.org/licenses/by/4.0/.

increasing delay time, as the population equilibrates, we find a shift of the response towards the 1s-2p transition energy, stemming from excitons in the ground state. The rise time of this resonance is a direct measure of relaxation from free to bound states. In PAPER I we further discuss the different spectral features and the comparison with experiments. This study shows that the developed theoretical approach presents a powerful tool, for the investigation of exciton relaxation dynamics and can be applied to a wide range of excitonic systems. In particular, we applied the same approach to model the exciton dynamics in a van-der-Waals heterostructure, consisting of two different monolayers, published in PAPER XII and XVI.

## 6.3 Phonon-assisted Luminescence from Dark Excitons

Monolayer materials, apart from their large potential for innovative technologies, remain in the focus of fundamental condensed matter research, because the strong many-particle interactions in these systems provide an excellent platform to study intriguing quantum phenomena of correlated systems. One of the major puzzles of the TMD research is the low-temperature photoluminescence (PL), which exhibits a plenitude of emission peaks below the apparent exciton ground states resonance [80–83]. The microscopic origin of these low temperature emissions features is to large extend unknown. Most studies on this topic have so far focused on the impact of bound exciton congurations, such as trions [84], biexcitons [85] and trapped excitons [86, 87], while the potential influence of indirect phonon-assisted recombination of intrinsically dark exciton states has been ignored to a large extend. Momentum indirect excitons are considered as dark since momentum conservation forbids the radiative decay of an exciton with non-zero centre of mass momentum. However, the simultaneous emission of a phonon, carrying away the exciton momentum, enables an indirect radiative decay of momentum dark excitons. In particular, in so called indirect semiconductors, where momentum indirect states are energetically more favourable then the bright state (direct transition), the luminescence at low temperatures can exhibit strong phonon-assisted PL signals resulting from the large population of dark states. Figure 7 illustrates the excitonic band diagram and the associated processes of this mechanism.

While the direct radiative decay of bright excitons has been extensively studied in previous works [88, 89], the theoretical description of the simultaneous phonon and photon interaction has remained challenging because of the non-markovian nature of these processes [90–92]. Based on the theoretical framework presented in this thesis, we derive a set of coupled equations of motion for the photon number $\langle B^\dagger B\rangle$, the photon-assisted polarization $\langle B^\dagger X_\mu\rangle$, the photon- and phonon-assisted polarization $\langle B^\dagger b^\dagger X_\mu\rangle$, exciton-phonon correlations $\langle B^\dagger X_\mu^\dagger X_\nu\rangle$, as well as higher order exciton-phonon and -photon correlations giving rise to a dephasing of the before mentioned central quantities. In PAPER III we present the full set of equations of motion and discuss the central approximations made in the derivation. Due to the large amount of degrees of freedom in these equations, a numerical evaluation would require

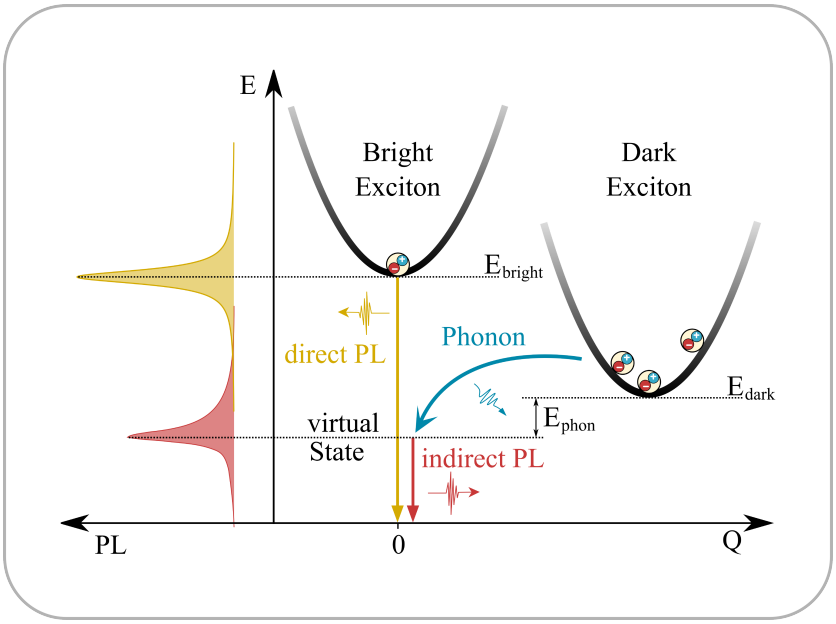


Figure 7: Luminescence from dark excitons. Sketch of direct and indirect decay channels showing the underlying scattering processes in the excitonic center-of-mass dispersion (right) and the corresponding PL signals (left). Momentum-dark excitons can decay by simultaneously interacting with phonons and photon, giving rise to phonon side peaks (red).

large computational resources and time, which is not very reasonable for this purpose. However, the empirical knowledge about the different time scales in our system, we can find an analytical expression for the luminescence spectrum. Since the exciton and phonon occupation numbers, after an ultrafast initial equilibration, change slowly compared to the dephasing times, we can obtain the static luminescence signal by solving the equations in the adiabatic limit. For the perpendicular emission from the monolayer we find the following closed expression for the luminescence spectrum

$$\begin{aligned} I_\sigma(\omega) &= \frac{2}{\hbar}\sum_\mu \frac{|M_\sigma^\mu|^2}{(E_{\mathbf{0}}^\mu-\omega)^2+(\Gamma_\mu^{\mathrm{rad}}+\Gamma_\mu^{\mathrm{ph}})^2}\Bigg(\Gamma_\mu^{\mathrm{rad}}N_{\mathbf{0}}^\mu \\ &+ \sum_{\nu\mathbf{q},\alpha\pm}|D_{\alpha\mathbf{q}}^{\mu\nu}|^2 N_{\mathbf{q}}^\nu\left(\frac{1}{2}\pm\frac{1}{2}+n_{\alpha\mathbf{q}}\right)\frac{\Gamma_{\nu\mathbf{q}}^{\mathrm{ph}}}{(E_{\mathbf{q}}^\nu\mp\Omega_{\mathbf{q}}^\alpha-\omega)^2+(\Gamma_{\nu\mathbf{q}}^{\mathrm{ph}})^2}\Bigg), \end{aligned} \tag{6.7}$$

where $N$ and $n$ are the exciton and phonon occupation numbers, respectively. Figure 8 shows calculated PL spectra for hBN-encapsulated monolayer WSe2 at dierent temperatures. The full spectra calculated from Eq. 6.7 are colour shaded, whereas the solid lines represent the result for $\Gamma^{\mathrm{ph}}_{\nu\mathbf{q}}$, i.e. requiring exact energy conservation.

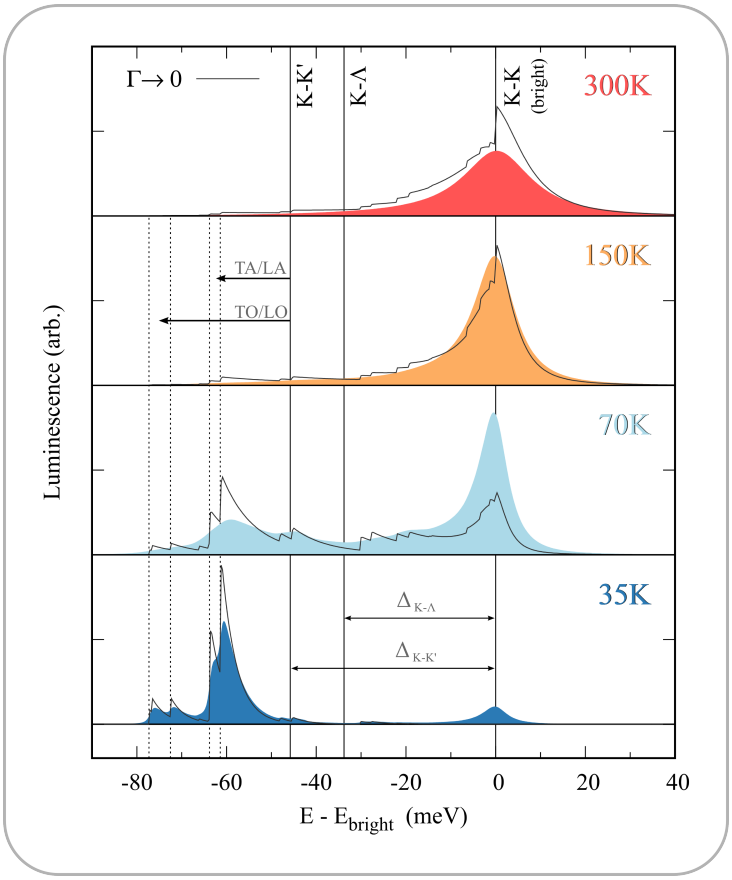


Figure 8: Temperature dependent PL. Calculated PL spectra of hBN-encapsulated $WSe_2$ monolayers for four temperatures. Together with the calculation from Eq. 6.7 (coloured curves) we also show the corresponding Fermis golden rule solution (thin solid lines). While at higher temperatures, the spectrum is dominated by an asymmetrically broadened bright state resonance, cryogenic temperatures give rise to strong indirect peaks stemming from the phonon-assisted recombination of dark excitons.

Therefore the sharp steps in the solid line conveniently illustrate the mul-

titude of exciton valleys and phonon modes involved in the PL spectrum. Each step corresponds to transitions from the minimum of a certain valley by absorbing or emitting a phonon. At 300 K and 150 K the PL only shows one main peak at the bright exciton resonance. However, the peak is asymmetrically broadened due to phonon-assisted recombinations of dark states (denoted with KK and K$\Lambda$) below the bright exciton. At lower temperatures the optical the emission shifts towards several indirect PL peaks below the bright exciton. These peaks result from the phonon-assisted recombination of the lowest lying K-K exciton. The predicted temperature behaviour as well as the observed low temperature PL peaks at about -60 meV (K-K - acoustic phonon assisted) and -75 meV (K-K - optical phonon assisted) agree well with experimental observations [80–83]. Although these peaks have been clearly observed in several independent measurements on hBN encapsulated samples, they were to a large extent ignored in literature due to their unclear origin. Our work ascribes these peaks to signatures of indirect phonon-assisted transitions from lower lying momentum-dark excitons in tungsten-based TMDs. In PAPER III, we show a direct comparison between experiment and theory and also analyse and explain the differences in the emission properties of tungsten- and molybdenum based monolayers.

# 7 Outlook – Heterostructures

After the intense research on monolayer materials, producing thousands of publications per year, most of the microscopic mechanisms guiding the characteristics of these materials are quite well understood and first prototypes of detectors and transistors based on TMDs have already been demonstrated. Therefore the research focus has recently shifted towards more complex systems, such as so called hetero-bilayers. These are comprised of two different monolayers materials stacked on top of each other, which only weekly interact through Van-der-Waals forces. For example, stacking two monolayers with different work functions gives rise to an atomically sharp p-n-junction. As we have demonstrated in PAPER XVI the optical excitation of one layer is followed by an ultrafast charge separation, giving rise to interlayer excitons with electron and hole residing in different layers. The energetic structure and the dynamics of interlayer excitons can easily be tailored by combining different materials and substrates, which enables a whole new play ground for physical phenomena and possible applications. One particularly interesting topic, which we will consider in our future studies, is the impact of lattice mismatches between the two monolayers.

Due to the different periodicities of the stacked monolayers, the physics of the heterostructure will be guided by the emergence of super-cells or so called Moire patterns, characterizing the periodicity of the overall system. Particularly appealing about these moire patterns, is that their seize can be controlled by changing the stacking angel. Together with the freedom of choice for the underlying monolayer materials, this tunability of properties gives rise to a completely new field in nano electronics, nowadays in literature already referred to as twistronics. In our future studies, we will focus on the theoretical description of moire patterns and their impact on exciton formation and relaxation dynamics.

# Acknowledgments

I sincerely want to thank all the people who enabled me to write this thesis. First of all, I would like to thank my supervisor Ermin Malic for his patience and the outstanding support over the last years. I also thank my examiner Jari Kinaret for his helpful comments and advices. I thank Paul Erhart for supporting me as second supervisor and Bo Hellsing for reviewing my thesis. Furthermore, I would like to thank the whole work group at Chalmers and the TU Berlin for all the fruitful discussions. Last but not least, I would like to express my cordial thanks to my family, friends and my partner Lea Käbitz for encouraging me and being there in good and not so good times.

# References


[1] Bader, S. & Parkin, S. Spintronics. *Annu. Rev. Condens. Matter Phys.* **1**, 71–88 (2010).

[2] Schaibley, J. R. *et al.* Valleytronics in 2d materials. *Nature Reviews Materials* **1**, 16055 (2016).

[3] Mas-Balleste, R., Gomez-Navarro, C., Gomez-Herrero, J. & Zamora, F. 2d materials: to graphene and beyond. *Nanoscale* **3**, 20–30 (2011).

[4] Butler, S. Z. *et al.* Progress, challenges, and opportunities in two-dimensional materials beyond graphene. *ACS Nano* **7**, 2898–2926 (2013).

[5] Manzeli, S., Ovchinnikov, D., Pasquier, D., Yazyev, O. V. & Kis, A. 2d transition metal dichalcogenides. *Nature Reviews Materials* **2**, 17033 (2017).

[6] Geim, A. K. & Grigorieva, I. V. Van der waals heterostructures. *Nature* **499**, 419–425 (2013).

[7] Mak, K. F., Lee, C., Hone, J., Shan, J. & Heinz, T. F. Atomically thin $MoS_2$: A new direct-gap semiconductor. *Phys. Rev. Lett.* **105**, 136805 (2010).

[8] Wang Qing Hua, Kalantar-Zadeh Kourosh, Kis Andras, Coleman Jonathan N. & Strano Michael S. Electronics and optoelectronics of two-dimensional transition metal dichalcogenides. *Nature Nanotechnology* **7**, 699–712 (2012).

[9] Pospischil, A. & Mueller, T. Optoelectronic devices based on atomically thin transition metal dichalcogenides. *Applied Sciences* **6**, 78 (2016).

[10] Mak, K. F. & Shan, J. Photonics and optoelectronics of 2d semiconductor transition metal dichalcogenides. *Nature Photonics* **10**, 216–226 (2016).

[11] Mueller, T. & Malic, E. Exciton physics and device application of two-dimensional transition metal dichalcogenide semiconductors. *npj 2D Materials and Applications* **2**, 29 (2018).

[12] Wang, G. *et al.* Colloquium: Excitons in atomically thin transition metal dichalcogenides. *Reviews of Modern Physics* **90**, 021001 (2018).

[13] Ramasubramaniam, A. Large excitonic effects in monolayers of molybdenum and tungsten dichalcogenides. *Physical Review B* **86**, 115409 (2012).

[14] He, K. *et al.* Tightly bound excitons in monolayer $WSe_2$. *Physical Review Letters* **113**, 026803 (2014).

[15] Ugeda, M. M. *et al.* Giant bandgap renormalization and excitonic effects in a monolayer transition metal dichalcogenide semiconductor. *Nature Materials* **13**, 1091 (2014).

[16] Chernikov, A. *et al.* Exciton binding energy and nonhydrogenic rydberg series in monolayer $WS_2$. *Physical Review Letters* **113**, 076802 (2014).

[17] Hill, H. M. *et al.* Observation of excitonic rydberg states in monolayer $MoS_2$ and $WS_2$ by photoluminescence excitation spectroscopy. *Nano Letters* **15**, 2992–2997 (2015).

[18] Steinhoff, A. *et al.* Efficient excitonic photoluminescence in direct and indirect band gap monolayer $MoS_2$. *Nano Letters* **15**, 6841–6847 (2015).

[19] Stier, A. V. *et al.* Magnetooptics of exciton rydberg states in a monolayer semiconductor. *Physical Review Letters* **120**, 057405 (2018).

[20] Robert, C. *et al.* Optical spectroscopy of excited exciton states in $MoS_2$ monolayers in van der waals heterostructures. *Physical Review Materials* **2**, 011001 (2018).

[21] Pöllmann, C. *et al.* Resonant internal quantum transitions and femtosecond radiative decay of excitons in monolayer $WSe_2$. *Nature Materials* **14**, 889–893 (2015).

[22] Rasmussen, F. A. & Thygesen, K. S. Computational 2d materials database: electronic structure of transition-metal dichalcogenides and oxides. *The Journal of Physical Chemistry C* **119**, 13169–13183 (2015).

[23] Kormányos, A. *et al.* k· p theory for two-dimensional transition metal dichalcogenide semiconductors. *2D Materials* **2**, 022001 (2015).

[24] Yao, W., Xiao, D. & Niu, Q. Valley-dependent optoelectronics from inversion symmetry breaking. *Phys. Rev. B* **77**, 235406 (2008).

[25] Zeng Hualing, Dai Junfeng, Yao Wang, Xiao Di & Cui Xiaodong. Valley polarization in $MoS_2$ monolayers by optical pumping. *Nature Nanotechnology* **7**, 490–493 (2012).

[26] Cao, Ting *et al.* Valley-selective circular dichroism of monolayer molybdenum disulphide. *Nature Communications* **3**, 887 (2012).

[27] Xu Xiaodong, Yao Wang, Xiao Di & Heinz Tony F. Spin and pseudospins in layered transition metal dichalcogenides. *Nature Physics* **10**, 343–350 (2014).

[28] Yu, T. & Wu, M. W. Valley depolarization due to intervalley and intravalley electron-hole exchange interactions in monolayer $MoS_2$. *Phys. Rev. B* **89**, 205303 (2014).

[29] Selig, Malte *et al.* Excitonic linewidth and coherence lifetime in monolayer transition metal dichalcogenides. *Nature Communications* **7**, 13279 (2016).

[30] Christiansen, D. *et al.* Phonon sidebands in monolayer transition metal dichalcogenides. *Physical Review Letters* **119**, 187402 (2017).

[31] Feierabend, M., Berghäuser, G., Knorr, A. & Malic, E. Proposal for dark exciton based chemical sensors. *Nature Communications* **8** (2017).

[32] Selig, M. *et al.* Dark and bright exciton formation, thermalization, and photoluminescence in monolayer transition metal dichalcogenides. *2D Materials* **5**, 035017 (2018).

[33] Malic, E. & Knorr, A. *Graphene and Carbon Nanotubes: Ultrafast Optics and Relaxation Dynamics* (Wiley-VCH, Berlin, 2013).

[34] Berghäuser, G. & Malic, E. Analytical approach to excitonic properties of $MoS_2$. *Phys. Rev. B* **89**, 125309 (2014).

[35] Xiao, D., Liu, G.-B., Feng, W., Xu, X. & Yao, W. Coupled spin and valley physics in monolayers of $MoS_2$ and other group-VI dichalcogenides. *Physical Review Letters* **108**, 196802 (2012).

[36] Cudazzo, P., Tokatly, I. V. & Rubio, A. Dielectric screening in two-dimensional insulators: Implications for excitonic and impurity states in graphane. *Phys. Rev. B* **84**, 085406 (2011).

[37] Chernikov, A. *et al.* Exciton binding energy and nonhydrogenic rydberg series in monolayer $WS_2$. *Phys. Rev. Lett.* **113**, 076802 (2014).

[38] Rytova, N. *Proc. MSU, Phys., Astron.* **3**, 30 (1967).

[39] Keldysh, L. *JETP Lett.* **29**, 658 (1979).

[40] Laturia, A., Van de Put, M. L. & Vandenberghe, W. G. Dielectric properties of hexagonal boron nitride and transition metal dichalcogenides: from monolayer to bulk. *npj 2D Materials and Applications* **2**, 6 (2018).

[41] Rossi, F. & Kuhn, T. Theory of ultrafast phenomena in photoexcited semiconductors. *Reviews of Modern Physics* **74**, 895 (2002).

[42] Kira, M. & Koch, S. Many-body correlations and excitonic effects in semiconductor spectroscopy. *Progress in Quantum Electronics* **30**, 155–296 (2006).

[43] Axt, V. M. & Kuhn, T. Femtosecond spectroscopy in semiconductors: a key to coherences, correlations and quantum kinetics. *Reports on Progress in Physics* **67**, 433 (2004).

[44] Haug, H. & Koch, S. W. *Quantum Theory of the Optical and Electronic Properties of Semiconductors* (World Scientific Publishing Co. Pre. Ltd., Singapore, 2004).

[45] Dirac, P. A. M. *The principles of quantum mechanics.* 27 (Oxford University Press, 1981).

[46] Harris, E. G. *A pedestrian approach to quantum field theory* (Courier Corporation, 2014).

[47] Mahan, G. D. *Many-particle physics* (Springer Science & Business Media, 2013).

[48] Vogel, W. & Welsch, D.-G. *Quantum optics* (John Wiley & Sons, 2006).

[49] Jin, Z., Li, X., Mullen, J. T. & Kim, K. W. Intrinsic transport properties of electrons and holes in monolayer transition-metal dichalcogenides. *Physical Review B* **90**, 045422 (2014).

[50] Kaasbjerg, K., Thygesen, K. S. & Jauho, A.-P. Acoustic phonon limited mobility in two-dimensional semiconductors: Deformation potential and piezoelectric scattering in monolayer mos 2 from first principles. *Physical Review B* **87**, 235312 (2013).

[51] Toyozawa, Y. Theory of line-shapes of the exciton absorption bands. *Progress of Theoretical Physics* **20**, 53–81 (1958).

[52] Ivanov, A. & Haug, H. Self-consistent theory of the biexciton optical nonlinearity. *Physical Review B* **48**, 1490 (1993).

[53] Katsch, F., Selig, M., Carmele, A. & Knorr, A. Theory of exciton–exciton interactions in monolayer transition metal dichalcogenides. *Physica Status Solidi (b)* **255**, 1800185 (2018).

[54] Kuper, C. G. & Whitfield, G. D. *Polarons and excitons* (Plenum Press, 1966).

[55] Kira, M. & Koch, S. W. *Semiconductor quantum optics* (Cambridge University Press, 2011).

[56] Chernikov, A., Ruppert, C., Hill, H. M., Rigosi, A. F. & Heinz, T. F. Population inversion and giant bandgap renormalization in atomically thin $WS_2$ layers. *Nature Photonics* **9**, 466 (2015).

[57] Cunningham, P. D., Hanbicki, A. T., McCreary, K. M. & Jonker, B. T. Photoinduced bandgap renormalization and exciton binding energy reduction in $WS_2$. *ACS Nano* **11**, 12601–12608 (2017).

[58] Steinhoff, A., Rosner, M., Jahnke, F., Wehling, T. & Gies, C. Influence of excited carriers on the optical and electronic properties of $MoS_2$. *Nano Letters* **14**, 3743–3748 (2014).

[59] Kaindl, R. A., Carnahan, M. A., Hägele, D., Lövenich, R. & Chemla, D. S. Ultrafast terahertz probes of transient conducting and insulating phases in an electron–hole gas. *Nature* **423**, 734–738 (2003).

[60] Kira, M., Hoyer, W. & Koch, S. Terahertz signatures of the exciton formation dynamics in non-resonantly excited semiconductors. *Solid State Communications* **129**, 733–736 (2004).

[61] Cha, S. *et al.* 1s-intraexcitonic dynamics in monolayer $MoS_2$ probed by ultrafast mid-infrared spectroscopy. *Nature Communications* **7**, 10768 (2016).

[62] Steinleitner, P. *et al.* Direct observation of ultrafast exciton formation in a monolayer of $WSe_2$. *Nano Letters* **17**, 1455–1460 (2017).

[63] Kira, M., Hoyer, W. & Koch, S. W. Microscopic theory of the semiconductor terahertz response. *Physica Status Solidi (b)* **238**, 443–450 (2003).

[64] Steiner, J., Kira, M. & Koch, S. W. Optical nonlinearities and Rabi flopping of an exciton population in a semiconductor interacting with strong terahertz fields. *Physical Review B* **77**, 165308 (2008).

[65] Koch, S., Kira, M., Khitrova, G. & Gibbs, H. Semiconductor excitons in new light. *Nature Materials* **5**, 523–531 (2006).

[66] Kira, M., Jahnke, F. & Koch, S. Microscopic theory of excitonic signatures in semiconductor photoluminescence. *Physical Review Letters* **81**, 3263 (1998).

[67] Feierabend, M. *et al.* Molecule signatures in photoluminescence spectra of transition metal dichalcogenides. *Physical Review Materials* **2**, 014004 (2018).

[68] Raja, A. *et al.* Coulomb engineering of the bandgap and excitons in two-dimensional materials. *Nature Communications* **8**, 15251 (2017).

[69] Singh, A. *et al.* Intrinsic homogeneous linewidth and broadening mechanisms of excitons in monolayer transition metal dichalcogenides. *Nature Communications* **6**, 8315 (2015).

[70] Palummo, M., Bernardi, M. & Grossman, J. C. Exciton radiative lifetimes in two-dimensional transition metal dichalcogenides. *Nano Letters* **15**, 2794–2800 (2015).

[71] Dey, P. *et al.* Optical coherence in atomic-monolayer transition-metal dichalcogenides limited by electron-phonon interactions. *Physical Review Letters* **116**, 127402 (2016).

[72] Niehues, I. *et al.* Strain control of exciton–phonon coupling in atomically thin semiconductors. *Nano Letters* **18**, 1751–1757 (2018).

[73] Khatibi, Z. *et al.* Impact of strain on the excitonic linewidth in transition metal dichalcogenides. *2D Materials* **6**, 015015 (2018).

[74] Knorr, A., Hughes, S., Stroucken, T. & Koch, S. Theory of ultrafast spatio-temporal dynamics in semiconductor heterostructures. *Chemical Physics* **210**, 27–47 (1996).

[75] Thränhardt, A., Kuckenburg, S., Knorr, A., Meier, T. & Koch, S. Quantum theory of phonon-assisted exciton formation and luminescence in semiconductor quantum wells. *Physical Review B* **62**, 2706 (2000).

[76] Geick, R., Perry, C. & Rupprecht, G. *Physical Review* **146**, 543 (1966).

[77] Kazimierczuk, T., Fröhlich, D., Scheel, S., Stolz, H. & Bayer, M. Giant rydberg excitons in the copper oxide $Cu_2O$. *Nature* **514**, 343 (2014).

[78] Stolz, H., Schöne, F. & Semkat, D. Interaction of rydberg excitons in cuprous oxide with phonons and photons: optical linewidth and polariton effect. *New Journal of Physics* **20**, 023019 (2018).

[79] Siantidis, K., Axt, V. & Kuhn, T. Dynamics of exciton formation for near band-gap excitations. *Physical Review B* **65**, 035303 (2001).

[80] Lindlau, J. *et al.* Identifying optical signatures of momentum-dark excitons in transition metal dichalcogenide monolayers. *arXiv preprint arXiv:1710.00988* (2017).

[81] Courtade, E. *et al.* Charged excitons in monolayer $WSe_2$: experiment and theory. *Physical Review B* **96**, 085302 (2017).

[82] Ye, Z. *et al.* Efficient generation of neutral and charged biexcitons in encapsulated $WSe_2$ monolayers. *Nature Communications* **9**, 3718 (2018).

[83] Barbone, M. *et al.* Charge-tuneable biexciton complexes in monolayer $WSe_2$. *Nature Communications* **9**, 3721 (2018).

[84] Mak, K. F. *et al.* Tightly bound trions in monolayer $MoS_2$. *Nature Materials* **12**, 207 (2013).

[85] Plechinger, G. *et al.* Identification of excitons, trions and biexcitons in single-layer $WS_2$. *Physica Status Solidi (RRL)–Rapid Research Letters* **9**, 457–461 (2015).

[86] Korn, T., Heydrich, S., Hirmer, M., Schmutzler, J. & Schüller, C. Low-temperature photocarrier dynamics in monolayer $MoS_2$. *Applied Physics Letters* **99**, 102109 (2011).

[87] Tonndorf, P. *et al.* Single-photon emission from localized excitons in an atomically thin semiconductor. *Optica* **2**, 347–352 (2015).

[88] Tonndorf, P. *et al.* Photoluminescence emission and raman response of monolayer $MoS_2$, $MoSe_2$, and $WSe_2$. *Optics Express* **21**, 4908–4916 (2013).

[89] Wang, H. *et al.* Radiative lifetimes of excitons and trions in monolayers of the metal dichalcogenide $MoS_2$. *Physical Review B* **93**, 045407 (2016).

[90] Feldtmann, T., Kira, M. & Koch, S. W. Phonon sidebands in semiconductor luminescence. *Physica Status Solidi (b)* **246**, 332–336 (2009).

[91] Feldtmann, T., Kira, M. & Koch, S. W. Theoretical analysis of higher-order phonon sidebands in semiconductor luminescence spectra. *Journal of Luminescence* **130**, 107–113 (2010).

[92] Chernikov, A. *et al.* Phonon-assisted luminescence of polar semiconductors: Fröhlich coupling versus deformation-potential scattering. *Physical Review B* **85**, 035201 (2012).

## Paper I

*Exciton Relaxation Cascade in two-dimensional Transition Metal Dichalcogenides*

S. Brem, M. Selig, G. Berghaeuser and E. Malic

Scientific reports 8.1: 8238 (2018)

## Paper II

*Intrinsic Lifetime of Higher Excitonic States in Tungsten Diselenide Monolayers*

S. Brem, J. Zipfel, M. Selig, A. Raja, L. Waldecker, J. Ziegler, T. Taniguchi, K. Watanabe, A. Chernikov, E. Malic

arXiv preprint arXiv:1904.04729 (2019)

## Paper III

*Phonon-assisted Photoluminescence from Dark Excitons in Monolayers of Transition Metal Dichalcogenides*

S. Brem, A. Ekman, D. Christiansen, F. Katsch, M. Selig, C. Robert, X. Marie, B. Urbaszek, A. Knorr, E. Malic

arXiv preprint arXiv:1904.04711 (2019)